Dichotomy property of dispersion equation of guided waves propagating in anisotropic composite plates

Shuanglin Guo, Marc Rebillat, Nazih Mechbal

Dichotomy property of dispersion equation of guided waves propagating in anisotropic composite plates

Shuanglin Guo, Marc Rebillat, Nazih Mechbal *

Procédés et Ingénierie en Mécanique et Matériaux, Arts et Métiers ParisTech, France

A B S T R A C T

Accurate prediction of dispersion curves for ultrasonic guided waves propagation in multi-layered composite laminates is crucial for the deployment of nondestructive testing procedures and structural health monitoring algorithms dedicated to aerospace composite materials. However, existing efforts mainly focused on finding ways to build complex-valued dispersion equations for guided waves (see transfer matrix method (TMM), global matrix method (GMM) and stiffness matrix method (SMM) for example) with little focus on developing efficient and stable numerical solving methods associated with the derived complex-valued equations. In this paper, the conditions under which complex-valued dispersion equations are either real- or purely imaginary-valued equations (termed as dichotomy property) are derived for both single- and multi-layered composite plates. With such a property, the complex-valued dispersion equations can be efficiently numerically solved within the real number field via the standard bisection method or the corrected phase change method. It is thus now possible to overcome numerical issues frequently reported in literature. Besides, a parallel computing technique is proposed in this paper to improve the computational efficiency of the traditional GMM. The proposed methodology provides a new standard framework to solve the dispersion equations which is stable, multipurpose, and numerically efficient.

1. Introduction

One important tendency in aerospace engineering is the increasing use of composite laminates benefiting from their high strength to weight ratios. Many Lamb wave-based structural health monitoring (SHM) techniques have been developed to detect and locate damage in composite materials such that the integrity and safety of the aerospace structures under service can be guaranteed [1,2]. Two basic characteristics of Lamb waves [3] establish the foundation of SHM for aerospace composite structures: (1) it can propagate to a long distance and cover a large monitoring area; (2) some propagating modes possess high sensitivity to a certain defect type occurring in composite materials, e.g., delamination, matrix cracking, fiber degradation and debonding, corrosion and fatigue fracture, etc. SHM algorithms however heavily rely on computational methods dedicated to dispersion curves prediction [4–10] allowing to link the phase velocity of a given mode with the excitation frequency. Dispersion curves are for example the basis for selecting appropriate excitation frequencies and designing an optimal piezoelectric transducer (PZT) network (position and size of the PZT elements) [11,12] or for advanced damage localization algorithms [13,14]. Accurately and efficiently computing dispersion curves is thus mandatory for the deployment of SHM to aerospace composite structures by means of Lamb waves. However, strong anisotropy and multiple layers stacking of composite laminates complicate the theory of guided wave propagation such that the conventional single-layered homogeneous and isotropic model, i.e., Rayleigh–Lamb equations [15], is no longer suitable for modeling

guided waves propagation in composite laminates. Therefore, for the derivation of such dispersion curves associated with guided waves propagation in anisotropic multi-layered plates matrix formulations have become the prevalent modeling techniques.

A first method is the transfer matrix method [5,16–18] (TMM) which relates the field variables, i.e., the stress and displacement components, at the top and bottom surfaces of the plate through a series of transfer matrices, and simultaneously take account for the continuity of field variables at interfaces of adjacent layers and the traction free boundary conditions at the two outer surfaces of the plate. But one fatal flaw of TMM is the notorious "*large fd problem*" which means that at the large product value of frequency f and layer thickness d, the dispersion curves obtained from the solutions of the dispersion equation built with TMM become unstable. The reason of this problem is attributed to the poor conditioning of the transfer matrices due to the coexisting growing and decaying wave types.

An alternative global matrix method (GMM) was proposed [6,19,20]. The principal idea of GMM is to assemble all the sub-matrices representing the continuity conditions of field variables in each layer into a global matrix, along with all layers' wave amplitudes to be determined by the traction free boundary conditions. The pioneering software *Disperse* [21] and a toolbox implemented in MATLAB called *ElasticMatrix* [22] are based on GMM. The main merit of GMM rests on its numerical stability even at large fd range but at the cost of heavy computational burden. However, some problems still exist for GMM for some applications such as missing roots or the production of outliers for some mode [23], limited computational capability making that it can only cope with laminates containing no more than 64 layers [24], and the incomplete functionality that it only deals with isotropic and transversely isotropic materials [22], thus restricting the wave propagation direction along materials' principal axes.

A stiffness matrix method (SMM) has been developed by recasting the layer's transfer matrix to form the stiffness matrix that relates the displacement to stress at the top and bottom side of a layer [25,26]. Then, the continuity conditions used in TMM and GMM are now transformed to recursive procedures from the first to the last layer in SMM to produce a global stiffness matrix of the whole plate. Finally, the traction free boundary condition is applied to the generated global stiffness matrix to obtain the dispersion equation. In order to get stable dispersion solutions, SMM and TMM have been combined to form the stiffness transfer matrix method (STMM) [27]. SMM has been adopted to compute the dispersion curves of anisotropic composites with 400 layers being a component of the rocket Ariane 6 [24]. It has thus been proved that SMM is unconditionally stable. But its shortcoming is the degeneration from conceptual simplicity in comparison with TMM and GMM.

Through the previous literature review, it can be recognized that even if significant efforts are carried out to find ways of building the dispersion equation via different methods, e.g., TMM, GMM and SMM, little work was conducted to study the property of the derived dispersion equation and to find efficient and stable associated numerical solving methods. In most references, once the derivation of dispersion equation is completed, one just says that *the solution to this equation usually requires a utilization of numerical methods* (see [5,6,17,18,28]), but little details are provided. The derived dispersion equation belongs to the family of complex-valued equations, which is more difficult to solve than a real-valued equation. Thus, the majority of methods mathematically transform the solving process to search the global minimal moduli of the dispersion function that should be zero in theory, termed as Min-Abs method in this paper. A representative example is the pioneering software *Disperse* which employed a path-dependent minimal moduli search strategy combined with the convergence criteria of checking the included phase angle of the complex-valued characteristic function that should be greater than 90° [21,29]. The toolbox *ElasticMatrix* makes use of MATLAB built-in function *fminbnd* to achieve the minimal moduli searching purpose [22]. Another complex strategy adopted by the software *Dispersion Calculator* is to check, in a small interval, both the occurrence of minimum moduli and sign change of the dispersion function (see Table I of [24]). Recently, Zhu et al. developed an iterative method to solve the dispersion equation by also coping with the modulus of the dispersion function, i.e., $|\mathfrak{D}(f,\xi)|$, which provides a strict convergence condition to distinguish the local and global minima [30]. In addition to the Min-Abs method introduced above, another interesting method is by consecutively monitoring the phase change of the dispersion function, which is actually evolved from the convergence criteria of *Disperse*. However, this method suffers from numerical instability issue when applied to multiple layered plates having 50 layers (see Fig. 7(c) of [20]). Note that amongst the mentioned methods, only *Disperse* and Zhu's method can tackle viscoelastic plate [31,32], which is not the focus of the current paper, i.e., pure elastic laminate.

In comparison with the multi-layered anisotropic system, the standard root-finding algorithms, e.g., bisection and Newton–Raphson, are widely used for the single-layered isotropic Rayleigh–Lamb dispersion equation. The solving process of the Rayleigh–Lamb equation is achieved by dividing the whole solution domain into three regions, i.e., region 1 of $v < c_T$, region 2 of $c_T < v < c_L$ and region 3 of $v > c_L$, where v is the phase velocity, and c_T and c_L are the velocities of transverse and longitudinal modes, respectively. Then in each region, the complex-valued Rayleigh–Lamb equation is derived to be a real one such that any standard root-finding algorithm can be easily called to solve it (see [33] and ch. 6.3 of [28]). Inspired by the strategy of solving the Rayleigh–Lamb equation introduced above, the same idea of converting the complex-valued equation to a real one, which can be easily solved via standard root-finding algorithms, has been applied here to the multi-layered anisotropic dispersion equation built with GMM, TMM and SMM. Finally an important property of dispersion equations, termed as dichotomy property in this paper, is demonstrated: they are either real- or purely imaginary-valued equations. On the basis of this property, it is shown that some numerical issues can be overcome and as a consequence the computational efficiency gets a great improvement.

The structure of this paper is outlined here. The dispersion equation for a single-layered monoclinic lamina is briefly derived in Section 2 and its dichotomy property is comprehensively studied in Section 3. Then, this property is extended to a multi-layered anisotropic system via GMM in Section 4. The ability to overcome some numerical issues with the dichotomy property is validated in Section 5. Discussion is given in Section 6 and the conclusions are drawn in Section 7.

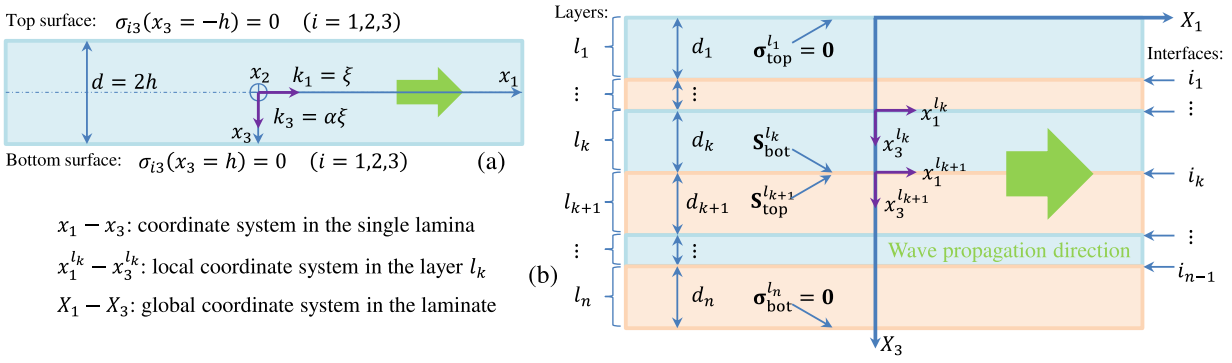

Fig. 1. Wave propagation model in (a) a single lamina and (b) a laminate.

2. Dispersion equation of guided wave in a monoclinic lamina

2.1. The basic equations for elastic solids

During the deformation of an elastic solid regardless of forced by a static or dynamic load, the 3D stress σ_{ij} and strain ε_{kl} tensors within the elastic solid are linked by the generalized Hooke's law as expressed using tensor notation in Eq. (1).

$$\sigma_{ij} = c_{ijkl}\varepsilon_{kl} \quad (i,j,k,l = 1,2,3) \tag{1}$$

where, c_{ijkl} is a fourth order tensor representative of elastic coefficients, which can be transformed to a six order matrix C_{pq} by using the Voigt notation with the one-to-one correspondence ij or $kl = 11, 22, 33, 23(32), 13(31), 12(21) \leftrightarrow p$ or $q = 1,2,3,4,5,6$ in order to facilitate the subsequent derivations.

Strain ε_{kl} and displacement u_i tensors are connected by the geometric equation presented in Eq. (2).

$$\varepsilon_{kl} = \frac{1}{2}(u_{k,l} + u_{l,k}) \quad (k,l = 1,2,3) \tag{2}$$

Given that guided waves propagation in a composite laminate is targeted here, a single lamina medium is studied firstly and then transition is made to a laminate. Considering the wave propagation model in a lamina (see Fig. 1(a)), which infinitely extends along axis x_2, the vibration of the lamina is inherently controlled by its elastodynamic equation as presented in Eq. (3) using tensor notation:

$$c_{ijkl}u_{l,kj} = \rho\ddot{u}_i \quad (i = 1,2,3) \tag{3}$$

where, ρ is the mass density.

Since the wave propagates along x_1-direction, the plane-strain state in x_2-direction is assumed thus leading to the displacement field being invariant to x_2. Besides, for a general time-harmonic wave solution of Eq. (3), the following displacement field $\mathbf{u}$ can be defined.

$$\mathbf{u} = [u_1,\ u_2,\ u_3]^{\mathrm{T}} = [U,\ V,\ W]^{\mathrm{T}} \mathrm{e}^{\mathrm{i}\xi(x_1 + \alpha x_3 - vt)} \tag{4}$$

where, T is the transpose operator; i is the imaginary number unit; ξ is the wavenumber along x_1 direction; α is the ratio of wavenumbers between x_3 and x_1 direction, as illustrated in Fig. 1; v is the phase velocity; U, V, W are the amplitudes of displacement along x_1, x_2, x_3 direction, respectively; t is the time variable. In order to focus on the subject of this article, i.e., dichotomy property of dispersion equations, classical results presented in Sections 2.2 and 2.3 will be directly provided because detailed contents already exists in many Refs. [2,34].

2.2. The Christoffel equation

Let us take a general monoclinic material into account. This kind of material has 13 independent constants in its elastic matrix $\mathbf{C}$, as presented in Eq. (5). For other kind of materials, such as orthotropic and isotropic materials, all the counterparts can be simplified from the corresponding equations of monoclinic material.

$$\begin{bmatrix}\sigma_{11}\\ \sigma_{22}\\ \sigma_{33}\\ \sigma_{23}\\ \sigma_{13}\\ \sigma_{12}\end{bmatrix} = \begin{bmatrix} C_{11} & C_{12} & C_{13} & 0 & 0 & C_{16} \\ & C_{22} & C_{23} & 0 & 0 & C_{26} \\ & & C_{33} & 0 & 0 & C_{36} \\ & & & C_{44} & C_{45} & 0 \\ & \text{sym} & & & C_{55} & 0 \\ & & & & & C_{66} \end{bmatrix} \begin{bmatrix}\varepsilon_{11}\\ \varepsilon_{22}\\ \varepsilon_{33}\\ 2\varepsilon_{23}\\ 2\varepsilon_{13}\\ 2\varepsilon_{12}\end{bmatrix} \tag{5}$$

Substituting Eqs. (4) and (5) into Eq. (3), the Christoffel equation $\mathbf{K}(\alpha)\mathbf{U}=\mathbf{0}$ can be generated as detailed in Eq. (6).

$$\begin{bmatrix} K_{11}(\alpha) & K_{12}(\alpha) & K_{13}(\alpha) \\ K_{12}(\alpha) & K_{22}(\alpha) & K_{23}(\alpha) \\ K_{13}(\alpha) & K_{23}(\alpha) & K_{33}(\alpha) \end{bmatrix} \begin{bmatrix} U \\ V \\ W \end{bmatrix} = \begin{bmatrix} 0 \\ 0 \\ 0 \end{bmatrix} \tag{6}$$

where,

$$\begin{aligned} &K_{11}(\alpha)=C_{11}-\rho v^2+C_{55}\alpha^2, \quad K_{12}(\alpha)=C_{16}+C_{45}\alpha^2, \quad K_{13}(\alpha)=(C_{13}+C_{55})\alpha, \\ &K_{22}(\alpha)=C_{66}-\rho v^2+C_{44}\alpha^2, \quad K_{23}(\alpha)=(C_{36}+C_{45})\alpha, \quad K_{33}(\alpha)=C_{55}-\rho v^2+C_{33}\alpha^2 \end{aligned} \tag{7}$$

To make sure that the above equation set leads to nontrivial amplitudes of displacement, the matrix $\mathbf{K}(\alpha)$ should be singular, namely, $\det\{\mathbf{K}(\alpha)\}=0$, where $\det\{\cdot\}$ means the operator of computing the determinant for a square matrix. Expanding this determinant results in a third order polynomial equation in terms of α^2 as expressed in Eq. (8).

$$\mathcal{A}(\alpha^2) \triangleq A_6\alpha^6+A_4\alpha^4+A_2\alpha^2+A_0=0 \tag{8}$$

where, the coefficients A_6, A_4, A_2, A_0 are presented in Appendix A, and can be computed from the constant elastic coefficients C_{pq} and mass density ρ at a specified phase velocity $v=v_0$.

$$\Delta=\frac{p^3}{27}+\frac{q^2}{4}, \quad p=\frac{3A_6A_2-A_4^2}{3A_6^2}, \quad q=\frac{27A_6^2A_0-9A_6A_4A_2+2A_4^3}{27A_6^3} \tag{9}$$

The three α^2 roots can be solved from Eq. (8) via Cardano's Formula or polynomial root-finding algorithm, for which their behavior is determined by the discriminant Δ defined in Eq. (9) according to the following three cases [20,35].

$$\begin{cases} (1) & \Delta<0, \text{ all } \alpha^2 \text{ roots are real and unique;} \\ (2) & \Delta=0, \text{ all } \alpha^2 \text{ roots are real and at least two are equal;} \\ (3) & \Delta>0, \text{ one } \alpha^2 \text{ root is real and the other two are complex conjugates.} \end{cases}$$

It is of great importance to state that the case $\Delta>0$ will be automatically excluded for isotropic materials (see ch. 5.6 of [28] for more information). Actually, the absence of $\Delta>0$ is not limited to isotropic materials, after a number of numerical investigations on various composite materials including transversely isotropic, orthotropic and monoclinic materials, only a few materials will lead to $\Delta>0$ in a small phase velocity range. That is to say, for most composite materials, the case $\Delta>0$ will be also automatically excluded. One convincing evidence catering this perspective comes from the Fig. 2 of [20]. In the following numerical examples, the existence of $\Delta>0$ will be checked firstly for the sake of strictness. For $\Delta\le 0$, the three α^2 roots are all real numbers and can be sorted in Eq. (10a). The six α roots regardless of which case are obtained by satisfying the condition in Eq. (10b).

$$\alpha_1^2\le\alpha_3^2\le\alpha_5^2, \quad \text{if } \Delta\le 0 \tag{10a}$$

$$\alpha_2=-\alpha_1,\ \alpha_4=-\alpha_3,\ \alpha_6=-\alpha_5 \tag{10b}$$

2.3. The displacement and stress fields

For each α_r $(r=1,\dots,6)$, there will be a corresponding solution of displacement amplitude $\left[U_r,\ V_r,\ W_r\right]^{\mathrm{T}}$ according to Eq. (6), which is one degree on indeterminacy according to the theory of linear algebra. The three displacement amplitudes can be determined by assigning a specific value for a certain term, for example $U_r=1$, and V_r and W_r are found from the resulted equation set via Cramer's Rule as presented in Eq. (11).

$$V_r=\frac{K_{11}(\alpha_r)K_{23}(\alpha_r)-K_{12}(\alpha_r)K_{13}(\alpha_r)}{K_{13}(\alpha_r)K_{22}(\alpha_r)-K_{12}(\alpha_r)K_{23}(\alpha_r)}, \quad W_r=\frac{K_{11}(\alpha_r)K_{23}(\alpha_r)-K_{12}(\alpha_r)K_{13}(\alpha_r)}{K_{12}(\alpha_r)K_{33}(\alpha_r)-K_{13}(\alpha_r)K_{23}(\alpha_r)} \tag{11}$$

It is easy to get the following relationship given the condition in Eq. (10b) if one substitutes the specific expression of $K_{ij}(\alpha)$ in Eq. (7) into Eq. (11).

$$V_2=V_1,\ V_4=V_3,\ V_6=V_5; \quad W_2=-W_1,\ W_4=-W_3,\ W_6=-W_5 \tag{12}$$

With the predefined form of displacements in Eq. (4) and the obtained amplitudes in Eq. (11), the displacement field $\mathbf{u}=[u_1,\ u_2,\ u_3]^{\mathrm{T}}$ now can be written as the superposition of the six solutions as shown in Eq. (13), in which each term within the summation represents a partial wave.

$$\begin{cases} u_1=\left(\sum_{r=1}^{6}\eta_r e^{\mathrm{i}\xi\alpha_r x_3}\right)e^{\mathrm{i}\xi(x_1-vt)} \\ u_2=\left(\sum_{r=1}^{6}\eta_r V_r e^{\mathrm{i}\xi\alpha_r x_3}\right)e^{\mathrm{i}\xi(x_1-vt)} \\ u_3=\left(\sum_{r=1}^{6}\eta_r W_r e^{\mathrm{i}\xi\alpha_r x_3}\right)e^{\mathrm{i}\xi(x_1-vt)} \end{cases} \tag{13}$$

where, η_r is the participation factor of partial wave to be determined, which can be organized into a vector $\boldsymbol{\eta}=[\eta_1,\ \eta_2,\ \eta_3,\ \eta_4,\ \eta_5,\ \eta_6]^{\mathrm{T}}$.

Following Eqs. (2), (5), and (13), the stress tensor defined in Eq. (1) can be written as the superposition of six partial waves as presented in Eq. (14), in which only the three terms $\boldsymbol{\sigma} = [\sigma_{33}, \sigma_{23}, \sigma_{13}]^{\mathrm{T}}$ are provided because they correspond to the boundary conditions at the bottom and top surfaces of a single lamina to be evaluated in the following section.

$$\begin{cases} \sigma_{33} = \left(\sum_{r=1}^{6} \eta_r \beta_{1r} \mathrm{e}^{\mathrm{i}\xi\alpha_r x_3}\right) \mathrm{i}\xi \mathrm{e}^{\mathrm{i}\xi(x_1 - vt)} \\ \sigma_{23} = \left(\sum_{r=1}^{6} \eta_r \beta_{2r} \mathrm{e}^{\mathrm{i}\xi\alpha_r x_3}\right) \mathrm{i}\xi \mathrm{e}^{\mathrm{i}\xi(x_1 - vt)} \\ \sigma_{13} = \left(\sum_{r=1}^{6} \eta_r \beta_{3r} \mathrm{e}^{\mathrm{i}\xi\alpha_r x_3}\right) \mathrm{i}\xi \mathrm{e}^{\mathrm{i}\xi(x_1 - vt)} \end{cases} \tag{14}$$

where, β_{ir} is the amplitude of partial wave in terms of stress and is defined in Eq. (15).

$$\begin{aligned} \beta_{1r} &= C_{13} + C_{36} V_r + C_{33} \alpha_r W_r \\ \beta_{2r} &= C_{45} \alpha_r + C_{44} \alpha_r V_r + C_{45} W_r \quad (r = 1, \ldots, 6) \\ \beta_{3r} &= C_{55} \alpha_r + C_{45} \alpha_r V_r + C_{55} W_r \end{aligned} \tag{15}$$

Like in Eq. (12), β_{ir} exhibits some relationships described in Eq. (16).

$$\begin{aligned} &\beta_{12} = \beta_{11}, \ \beta_{14} = \beta_{13}, \ \beta_{16} = \beta_{15} \\ &\beta_{22} = -\beta_{21}, \ \beta_{24} = -\beta_{23}, \ \beta_{26} = -\beta_{25} \\ &\beta_{32} = -\beta_{31}, \ \beta_{34} = -\beta_{33}, \ \beta_{36} = -\beta_{35} \end{aligned} \tag{16}$$

2.4. Dispersion equations of symmetric and anti-symmetric modes

The stress field should meet the traction free boundary condition (BC) as illustrated in Fig. 1(a) and formulated in Eq. (17) when guided waves propagate in a free plate. Furthermore, the displacement and stress fields have symmetry condition (SC) at the midplane of a lamina as presented in Eqs. (18a) and (18b) (see [5] for more information).

$$\sigma_{i3}(x_3 = \pm h) = 0 \quad (i = 1, 2, 3) \tag{17}$$

where, h is the half thickness.

$$u_3(x_3 = 0) = 0, \ \sigma_{23}(x_3 = 0) = \sigma_{13}(x_3 = 0) = 0 \quad \text{for symmetric modes} \tag{18a}$$

$$u_1(x_3 = 0) = u_2(x_3 = 0) = 0, \ \sigma_{33}(x_3 = 0) = 0 \quad \text{for anti-symmetric modes} \tag{18b}$$

Note that $x_3 = -h$ in Eq. (17) is redundant for deriving dispersion equations. Thus, we adopted the BC at $x_3 = h$ in Eq. (17) and the SC in Eq. (18a) to derive the dispersion equation of symmetric modes. Substituting Eqs. (13) and (14) into two equations, meanwhile reorganizing the resulted equation set in matrix form with the participation factors $\boldsymbol{\eta}$ being the unknown vector, one obtains Eq. (19).

$$\begin{bmatrix} W_1 & -W_1 & W_3 & -W_3 & W_5 & -W_5 \\ \beta_{21} & -\beta_{21} & \beta_{23} & -\beta_{23} & \beta_{25} & -\beta_{25} \\ \beta_{31} & -\beta_{31} & \beta_{33} & -\beta_{33} & \beta_{35} & -\beta_{35} \\ \beta_{11}\mathrm{e}^{\mathrm{i}\xi\alpha_1 h} & \beta_{11}\mathrm{e}^{-\mathrm{i}\xi\alpha_1 h} & \beta_{13}\mathrm{e}^{\mathrm{i}\xi\alpha_3 h} & \beta_{13}\mathrm{e}^{-\mathrm{i}\xi\alpha_3 h} & \beta_{15}\mathrm{e}^{\mathrm{i}\xi\alpha_5 h} & \beta_{15}\mathrm{e}^{-\mathrm{i}\xi\alpha_5 h} \\ \beta_{21}\mathrm{e}^{\mathrm{i}\xi\alpha_1 h} & -\beta_{21}\mathrm{e}^{-\mathrm{i}\xi\alpha_1 h} & \beta_{23}\mathrm{e}^{\mathrm{i}\xi\alpha_3 h} & -\beta_{23}\mathrm{e}^{-\mathrm{i}\xi\alpha_3 h} & \beta_{25}\mathrm{e}^{\mathrm{i}\xi\alpha_5 h} & -\beta_{25}\mathrm{e}^{-\mathrm{i}\xi\alpha_5 h} \\ \beta_{31}\mathrm{e}^{\mathrm{i}\xi\alpha_1 h} & -\beta_{31}\mathrm{e}^{-\mathrm{i}\xi\alpha_1 h} & \beta_{33}\mathrm{e}^{\mathrm{i}\xi\alpha_3 h} & -\beta_{33}\mathrm{e}^{-\mathrm{i}\xi\alpha_3 h} & \beta_{35}\mathrm{e}^{\mathrm{i}\xi\alpha_5 h} & -\beta_{35}\mathrm{e}^{-\mathrm{i}\xi\alpha_5 h} \end{bmatrix} \begin{bmatrix} \eta_1 \\ \eta_2 \\ \eta_3 \\ \eta_4 \\ \eta_5 \\ \eta_6 \end{bmatrix} = \begin{bmatrix} 0 \\ 0 \\ 0 \\ 0 \\ 0 \\ 0 \end{bmatrix} \tag{19}$$

Eq. (19) can be rewritten as a compact form, $\mathbf{D}_s(v, \xi)\boldsymbol{\eta} = \mathbf{0}$, where $\mathbf{D}_s$ is the matrix in Eq. (19) and the subscript 's' denotes the symmetric modes. It should be noted that in $\mathbf{D}_s$, in addition to ξ, there are yet variables α_r, W_r, β_{1r}, β_{2r}, β_{3r} ($r = 1, 3, 5$). But $\mathbf{D}_s$ implicitly links v and ξ given that α_r, W_r, β_{ir} are actually determined by v through the Christoffel equation. Thus, the dependency property on (v, ξ) has been attached to $\mathbf{D}_s$. In order to produce non-trivial solution of $\boldsymbol{\eta}$, $\mathbf{D}_s(v, \xi)$ should vanish as presented in Eq. (20), which is the dispersion equation for symmetric modes in implicit[1] form.

$$D_s(v, \xi) \triangleq \det\{\mathbf{D}_s(v, \xi)\} = 0 \quad \text{for symmetric modes} \tag{20}$$

For the dispersion equation of anti-symmetric modes, substituting Eqs. (13) and (14) into Eq. (17), with $x_3 = h$, and Eq. (18b) results in Eq. (21), which can be also rewritten as the compact form, $\mathbf{D}_a(v, \xi)\boldsymbol{\eta} = \mathbf{0}$, where the subscript '$a$' denotes the anti-symmetric modes. To guarantee a non-trivial solution of $\boldsymbol{\eta}$, $\mathbf{D}_a(v, \xi)$ should vanish as presented in Eq. (22), which is the dispersion equation for

[1] In this paper, the term *implicit* means that the dispersion equation is defined in matrix-determinant form.

anti-symmetric modes in implicit form.

$$\begin{bmatrix} 1 & 1 & 1 & 1 & 1 & 1 \\ V_1 & V_1 & V_3 & V_3 & V_5 & V_5 \\ \beta_{11} & \beta_{11} & \beta_{13} & \beta_{13} & \beta_{15} & \beta_{15} \\ \beta_{11}e^{i\xi\alpha_1 h} & \beta_{11}e^{-i\xi\alpha_1 h} & \beta_{13}e^{i\xi\alpha_3 h} & \beta_{13}e^{-i\xi\alpha_3 h} & \beta_{15}e^{i\xi\alpha_5 h} & \beta_{15}e^{-i\xi\alpha_5 h} \\ \beta_{21}e^{i\xi\alpha_1 h} & -\beta_{21}e^{-i\xi\alpha_1 h} & \beta_{23}e^{i\xi\alpha_3 h} & -\beta_{23}e^{-i\xi\alpha_3 h} & \beta_{25}e^{i\xi\alpha_5 h} & -\beta_{25}e^{-i\xi\alpha_5 h} \\ \beta_{31}e^{i\xi\alpha_1 h} & -\beta_{31}e^{-i\xi\alpha_1 h} & \beta_{33}e^{i\xi\alpha_3 h} & -\beta_{33}e^{-i\xi\alpha_3 h} & \beta_{35}e^{i\xi\alpha_5 h} & -\beta_{35}e^{-i\xi\alpha_5 h} \end{bmatrix} \begin{bmatrix} \eta_1 \\ \eta_2 \\ \eta_3 \\ \eta_4 \\ \eta_5 \\ \eta_6 \end{bmatrix} = \begin{bmatrix} 0 \\ 0 \\ 0 \\ 0 \\ 0 \\ 0 \end{bmatrix} \tag{21}$$

$$D_a(v,\xi) \triangleq \det\{\mathbf{D}_a(v,\xi)\} = 0 \quad \text{for anti-symmetric modes} \tag{22}$$

Observing Eqs. (19) and (21), it is certain that, no matter which SC is considered, $\mathbf{D}(v,\xi)$ is a complex-valued matrix due to the existence of complex exponential terms. In general, its determinant, $D(v,\xi)$, has real, $D^R(v,\xi)$, and imaginary, $D^I(v,\xi)$, parts. Thus, the intuitive way of solving the dispersion equation is to find the zero points of both parts and then take their intersections as presented in Eq. (23), which is easy to implement because both $D^R(v,\xi)$ and $D^I(v,\xi)$ are real-valued functions such that many real variables-based root-finding algorithms can be used such as the bisection method.

$$D(v,\xi) \triangleq D^R(v,\xi) + iD^I(v,\xi) = 0 \Leftrightarrow \begin{cases} D^R(v,\xi) = 0 \\ D^I(v,\xi) = 0 \end{cases} \tag{23}$$

The explicit[2] formula of the determinant of $\mathbf{D}_s(v,\xi)$ in Eq. (19) and $\mathbf{D}_a(v,\xi)$ in Eq. (21) were then derived in Eqs. (24a) and (24b) by right of the software *Mathematica* due to its powerful capability of symbolic computing. Note that during manipulation using *Mathematica*, the Euler's equation should be used, for example, $e^{i\xi\alpha_1 h} = \cos(\xi\alpha_1 h) + i\sin(\xi\alpha_1 h)$.

$$\begin{aligned} D_s(v,\xi) =& [B_1 \cos(\xi\alpha_1 h)\sin(\xi\alpha_3 h)\sin(\xi\alpha_5 h) + B_2 \sin(\xi\alpha_1 h)\cos(\xi\alpha_3 h)\sin(\xi\alpha_5 h) \\ &+ B_3 \sin(\xi\alpha_1 h)\sin(\xi\alpha_3 h)\cos(\xi\alpha_5 h)]B_4 \end{aligned} \tag{24a}$$

$$\begin{aligned} D_a(v,\xi) =& [B_1 \sin(\xi\alpha_1 h)\cos(\xi\alpha_3 h)\cos(\xi\alpha_5 h) + B_2 \cos(\xi\alpha_1 h)\sin(\xi\alpha_3 h)\cos(\xi\alpha_5 h) \\ &+ B_3 \cos(\xi\alpha_1 h)\cos(\xi\alpha_3 h)\sin(\xi\alpha_5 h)]B_5 \end{aligned} \tag{24b}$$

where,

$$\begin{aligned} B_1 &= \beta_{11}(\beta_{25}\beta_{33} - \beta_{23}\beta_{35}),\ B_2 = \beta_{13}(\beta_{21}\beta_{35} - \beta_{25}\beta_{31}),\ B_3 = \beta_{15}(\beta_{23}\beta_{31} - \beta_{21}\beta_{33}) \\ B_4 &= 8\left[W_1(\beta_{25}\beta_{33} - \beta_{23}\beta_{35}) + W_3(\beta_{21}\beta_{35} - \beta_{25}\beta_{31}) + W_5(\beta_{23}\beta_{31} - \beta_{21}\beta_{33})\right] \\ B_5 &= 8i\left[V_1(\beta_{15} - \beta_{13}) + V_3(\beta_{11} - \beta_{15}) + V_5(\beta_{13} - \beta_{11})\right] \end{aligned} \tag{25}$$

With Eqs. (24a) and (24b), the implicit dispersion equations, Eqs. (20) and (22), have been exposed in Eqs. (26a) and (26b). Considering that the tangent functions are discontinuous, it is preferred to adopt Eqs. (24a) and (24b) for computation.

$$B_1 \cot(\xi\alpha_1 h) + B_2 \cot(\xi\alpha_3 h) + B_3 \cot(\xi\alpha_5 h) = 0 \quad \text{for symmetric modes} \tag{26a}$$

$$B_1 \tan(\xi\alpha_1 h) + B_2 \tan(\xi\alpha_3 h) + B_3 \tan(\xi\alpha_5 h) = 0 \quad \text{for anti-symmetric modes} \tag{26b}$$

3. Dichotomy property of dispersion equation

In this section, we only focus on the case $\Delta \le 0$ to study the dichotomy property of dispersion equation through theoretical derivations, but we leave the extremely rare case $\Delta > 0$ to numerical validation in Section 5.2. There are three reasons for this: (1) the theoretical study on the case $\Delta \le 0$ is enough to show the essence of dichotomy property; (2) the theoretical derivation on the case $\Delta > 0$ is untractable, thus numerical validation is necessary; (3) the case $\Delta > 0$ is an extremely rare phenomenon for composite materials according to the explanation presented in Section 2.2.

3.1. Properties of intermediate parameters

For the case $\Delta \le 0$, all three α^2 roots are real numbers. Based on this, if $\alpha_r^2 \ge 0$ then $\alpha_r (= \pm\sqrt{\alpha_r^2})$ is a real number regardless of being positive or negative, while if $\alpha_r^2 < 0$ then α_r is a purely imaginary number. In order to investigate the dichotomy property of dispersion equations, three properties of the intermediate parameters V_r, W_r, β_{1r}, β_{2r}, β_{3r}, B_5 depending on α_r are listed below and the proof is provided in Appendix B.

[2] In this paper, the term *explicit* means that the dispersion equation is simplified from the original one defined in matrix-determinant form.

Property 1: $\alpha_r \in \mathbb{R} \implies (V_r, W_r, \beta_{1r}, \beta_{2r}, \beta_{3r}) \in \mathbb{R}^5$.
Property 2: $\alpha_r \in \mathrm{i}\mathbb{R} \implies (V_r, \beta_{1r}) \in \mathbb{R}^2$ and $(W_r, \beta_{2r}, \beta_{3r}) \in \mathrm{i}\mathbb{R}^3$.
Property 3: $\forall \alpha_r, B_5 \in \mathrm{i}\mathbb{R}$.

When the six roots of Eq. (8) are obtained for a specific material and v_0, one can sort them to satisfy the condition in Eq. (10a) ($\alpha_1^2 \le \alpha_3^2 \le \alpha_5^2$). This leads to the following four cases:

$$\begin{cases} (1) & \text{all } \alpha_1,\ \alpha_3,\ \alpha_5 \text{ are real numbers } \left(0 \le \alpha_1^2 \le \alpha_3^2 \le \alpha_5^2\right); \\ (2) & \text{only } \alpha_1 \text{ is a purely imaginary number } \left(\alpha_1^2 < 0 \le \alpha_3^2 \le \alpha_5^2\right); \\ (3) & \text{only } \alpha_1,\ \alpha_3 \text{ are purely imaginary numbers } \left(\alpha_1^2 \le \alpha_3^2 < 0 \le \alpha_5^2\right); \\ (4) & \text{all } \alpha_1,\ \alpha_3,\ \alpha_5 \text{ are purely imaginary numbers } \left(\alpha_1^2 \le \alpha_3^2 \le \alpha_5^2 < 0\right). \end{cases}$$

It is obvious that the boundary of the four cases is $\alpha_1 = 0$, $\alpha_3 = 0$, $\alpha_5 = 0$, respectively, which can be reached by letting $A_0 = 0$ in Eq. (8). Keeping in mind the expression of A_0 in Appendix A, this further leads to the definition of three critical velocities, which characterize the three bulk wave velocities (longitudinal, shear horizontal and shear vertical modes) propagating along the lamina plane. Note that dispersion equation has a singularity at the bulk wave velocity, thus, some outliers in the dispersion solutions will occur. For example, the constant phase velocities appearing in Fig. 3 of [23] and produced by the software *Disperse* can be interpreted as one of these outliers.

$$v_{\mathrm{I}} = \sqrt{\frac{A + \sqrt{B}}{2\rho}}, \quad v_{\mathrm{II}} = \sqrt{\frac{A - \sqrt{B}}{2\rho}}, \quad v_{\mathrm{III}} = \sqrt{\frac{C_{55}}{\rho}} \tag{27}$$

where, $A = C_{11} + C_{66}$ and $B = (C_{11} - C_{66})^2 + 4C_{16}^2$.

3.2. Dichotomy property of dispersion equation when sweeping ξ

In this section, we take the example of anti-symmetric modes to theoretically study the dichotomy property of dispersion equations. The tools used for anti-symmetric modes are readily applicable to symmetric modes.

3.2.1. Case 1: all α_1, α_3, α_5 are real numbers

For case 1, according to Property 1, all β_{1r}, β_{2r}, β_{3r} $(r = 1, 3, 5)$ are real numbers. The three coefficients B_1, B_2, B_3 defined in Eq. (25) are real numbers as well. Besides, set $B_5 = \mathrm{i}P_5$ where P_5 is a real number according to the Property 3. Thus, the dispersion function $\mathcal{D}_a(v, \xi)$ defined in Eq. (24b) can be written as follows.

$$\begin{aligned} \mathcal{D}_a(v,\xi) = \mathrm{i}[&B_1 \sin(\xi\alpha_1 h)\cos(\xi\alpha_3 h)\cos(\xi\alpha_5 h) + B_2 \cos(\xi\alpha_1 h)\sin(\xi\alpha_3 h)\cos(\xi\alpha_5 h) \\ &+ B_3 \cos(\xi\alpha_1 h)\cos(\xi\alpha_3 h)\sin(\xi\alpha_5 h)]P_5 = \mathrm{i}D_a^I(v,\xi) \Rightarrow \textbf{a purely imag. quantity} \end{aligned} \tag{28}$$

It is evident from Eq. (28) that $\mathcal{D}_a(v, \xi)$ should be a purely imaginary-valued function in case 1 given that all the terms in this function are real numbers other than the imaginary number unit. This is equivalent to say that its real part is identically vanishing, $\mathcal{D}_a^R(v, \xi) \equiv 0$. Thus, the original complex-valued equation $\mathcal{D}_a(v, \xi) = 0$ now has been transformed to $\mathcal{D}_a^I(v, \xi) = 0$, which is a real-valued equation easy to be solved via bisection method. This phenomenon casts the essence of dichotomy property.

3.2.2. Case 2: only α_1 is a purely imaginary number

In this case, set $\alpha_1 = \mathrm{i}a_1$. According to the Property 2 and 3, β_{21}, β_{31}, B_5 become purely imaginary numbers, so one can set them as $\beta_{21} = \mathrm{i}p_{21}$, $\beta_{31} = \mathrm{i}p_{31}$, $B_5 = \mathrm{i}P_5$, here a_1, p_{21}, p_{31}, P_5 are real numbers. In that way, B_1, B_2, B_3 in Eq. (25) can be deduced as follows.

$$\begin{aligned} B_1 &= \beta_{11}(\beta_{25}\beta_{33} - \beta_{23}\beta_{35}) \Rightarrow \text{a real number} \\ B_2 &= \beta_{13}(\mathrm{i}p_{21}\beta_{35} - \beta_{25}\mathrm{i}p_{31}) = \mathrm{i}\beta_{13}(p_{21}\beta_{35} - \beta_{25}p_{31}) = \mathrm{i}P_2 \Rightarrow \text{an imag. number} \\ B_3 &= \beta_{15}(\beta_{23}\mathrm{i}p_{31} - \mathrm{i}p_{21}\beta_{33}) = \mathrm{i}\beta_{15}(\beta_{23}p_{31} - p_{21}\beta_{33}) = \mathrm{i}P_3 \Rightarrow \text{an imag. number} \end{aligned} \tag{29}$$

where, P_2, P_3 are definitely real numbers.

With the new definitions, keeping in mind that $\sin(\mathrm{i}\xi a_1 h) = \mathrm{i}\sinh(\xi a_1 h)$, $\cos(\mathrm{i}\xi a_1 h) = \cosh(\xi a_1 h)$, where $\sinh(\cdot)$ and $\cosh(\cdot)$ is the hyperbolic sine and cosine function, respectively, $\mathcal{D}_a(v, \xi)$ defined in Eq. (24b) can be deduced as follows.

$$\begin{aligned} \mathcal{D}_a(v,\xi) = -[&B_1 \sinh(\xi a_1 h)\cos(\xi\alpha_3 h)\cos(\xi\alpha_5 h) + P_2 \cosh(\xi a_1 h)\sin(\xi\alpha_3 h)\cos(\xi\alpha_5 h) \\ &+ P_3 \cosh(\xi a_1 h)\cos(\xi\alpha_3 h)\sin(\xi\alpha_5 h)]P_5 \Rightarrow \textbf{a real quantity} \end{aligned} \tag{30}$$

This result reveals that in case 2, the imaginary part is identically vanishing, $\mathcal{D}_a^I(v, \xi) \equiv 0$. Thus, the original complex-valued equation $\mathcal{D}_a(v, \xi) = 0$ now has been converted to $\mathcal{D}_a^R(v, \xi) = 0$, which is a real-valued equation easy to be solved via bisection method.

Table 1
The ranges of phase velocity v [m/s] that correspond to the four cases.

Case 1	Case 2	Case 3	Case 4
$0 \le \alpha_1^2 \le \alpha_3^2 \le \alpha_5^2$	$\alpha_1^2 < 0 \le \alpha_3^2 \le \alpha_5^2$	$\alpha_1^2 \le \alpha_3^2 < 0 \le \alpha_5^2$	$\alpha_1^2 \le \alpha_3^2 \le \alpha_5^2 < 0$
[8918.75, +∞)	[2142.25, 8918.75)	[1879.72, 2142.25)	(0, 1879.72)

3.2.3. Case 3: only α_1, α_3 are purely imaginary numbers

In this case, set $\alpha_1 = \mathrm{i}a_1$, $\alpha_3 = \mathrm{i}a_3$, meanwhile according to the Property 2 and 3, set $\beta_{21} = \mathrm{i}p_{21}$, $\beta_{31} = \mathrm{i}p_{31}$, $\beta_{23} = \mathrm{i}p_{23}$, $\beta_{33} = \mathrm{i}p_{33}$, $B_5 = \mathrm{i}P_5$, where a_1, a_3, p_{21}, p_{31}, p_{23}, p_{33}, P_5 are real numbers. With the new substitutions, B_1, B_2, B_3 in Eq. (25) can be deduced as follows.

$$\begin{aligned} B_1 &= \beta_{11}(\beta_{25}\mathrm{i}p_{33} - \mathrm{i}p_{23}\beta_{35}) = \mathrm{i}\beta_{11}(\beta_{25}p_{33} - p_{23}\beta_{35}) = \mathrm{i}P_1 \Rightarrow \text{an imag. number} \\ B_2 &= \beta_{13}(\mathrm{i}p_{21}\beta_{35} - \beta_{25}\mathrm{i}p_{31}) = \mathrm{i}\beta_{13}(p_{21}\beta_{35} - \beta_{25}p_{31}) = \mathrm{i}P_2 \Rightarrow \text{an imag. number} \\ B_3 &= \beta_{15}(\mathrm{i}p_{23}\mathrm{i}p_{31} - \mathrm{i}p_{21}\mathrm{i}p_{33}) = \beta_{15}(-p_{23}p_{31} + p_{21}p_{33}) \Rightarrow \text{a real number} \end{aligned} \tag{31}$$

where, P_1, P_2 are definitely real numbers.

Substitute Eq. (31) into Eq. (24b) to lead to the following form. Obviously, as with case 1, the solving process should be focused on the imaginary part in case 3, $D_a^I(v,\xi) = 0$.

$$\begin{aligned} D_a(v,\xi) =& \mathrm{i}[-P_1 \sinh(\xi a_1 h)\cosh(\xi a_3 h)\cos(\xi\alpha_5 h) - P_2 \cosh(\xi a_1 h)\sinh(\xi a_3 h)\cos(\xi\alpha_5 h) \\ &+ B_3 \cosh(\xi a_1 h)\cosh(\xi a_3 h)\sin(\xi\alpha_5 h)]P_5 \Rightarrow \textbf{a purely imag. quantity} \end{aligned} \tag{32}$$

3.2.4. Case 4: all α_1, α_3, α_5 are purely imaginary numbers

In this case, set $\alpha_1 = \mathrm{i}a_1$, $\alpha_3 = \mathrm{i}a_3$, $\alpha_5 = \mathrm{i}a_5$, according to the Property 2 and 3, continuously set $\beta_{21} = \mathrm{i}p_{21}$, $\beta_{31} = \mathrm{i}p_{31}$, $\beta_{23} = \mathrm{i}p_{23}$, $\beta_{33} = \mathrm{i}p_{33}$, $\beta_{25} = \mathrm{i}p_{25}$, $\beta_{35} = \mathrm{i}p_{35}$, $B_5 = \mathrm{i}P_5$, where, a_1, a_3, a_5, p_{21}, p_{31}, p_{23}, p_{33}, p_{25}, p_{35}, P_5 are real numbers. Substitute these new settings into Eq. (25) to deduce as follows.

$$\begin{aligned} B_1 &= \beta_{11}(\mathrm{i}p_{25}\mathrm{i}p_{33} - \mathrm{i}p_{23}\mathrm{i}p_{35}) = \beta_{11}(-p_{25}p_{33} + p_{23}p_{35}) \Rightarrow \text{a real number} \\ B_2 &= \beta_{13}(\mathrm{i}p_{21}\mathrm{i}p_{35} - \mathrm{i}p_{25}\mathrm{i}p_{31}) = \beta_{13}(-p_{21}p_{35} + p_{25}p_{31}) \Rightarrow \text{a real number} \\ B_3 &= \beta_{15}(\mathrm{i}p_{23}\mathrm{i}p_{31} - \mathrm{i}p_{21}\mathrm{i}p_{33}) = \beta_{15}(-p_{23}p_{31} + p_{21}p_{33}) \Rightarrow \text{a real number} \end{aligned} \tag{33}$$

Under the new settings, Eq. (24b) can be further deduced to Eq. (34). Hence, case 4 has the same dichotomy property as with case 2, i.e., the solving process should be focused on the real part, $D_a^R(v,\xi) = 0$.

$$\begin{aligned} D_a(v,\xi) =& -[B_1 \sinh(\xi a_1 h)\cosh(\xi a_3 h)\cosh(\xi a_5 h) + B_2 \cosh(\xi a_1 h)\sinh(\xi a_3 h)\cosh(\xi a_5 h) \\ &+ B_3 \cosh(\xi a_1 h)\cosh(\xi a_3 h)\sinh(\xi a_5 h)]P_5 \Rightarrow \textbf{a real quantity} \end{aligned} \tag{34}$$

3.2.5. Numerical validation of the dichotomy property when sweeping ξ

The chosen structure is a single-layered monoclinic plate, whose material properties are cited from [20] and provided in Appendix D for convenience. The absence of $\Delta > 0$ has been checked in the Fig. 2(d) of [20] that shows the three real-valued α^2 roots. With the provided material properties, the three critical velocities can be computed based on Eq. (27), which, therefore, divide the whole domain of phase velocity v into four ranges that correspond to the four cases presented in Table 1.

Analysis of Case 1:

Firstly, we assign a typical phase velocity $v_0 = 9000\,\mathrm{m/s}$ according to Table 1, and substitute the specified material parameters into Eq. (A.1) to calculate the polynomial coefficients of Eq. (8). Then, the three α^2 roots of the bi-cubic equation, $\mathcal{A}(\alpha^2) = 0$, can be solved via Cardano's Formula, from which the six α roots are finally obtained with the three predominant ones being $\alpha_1 = 0.5667$, $\alpha_3 = 3.2007$, $\alpha_5 = 5.8644$. All the three terms are real numbers, which is in agreement with the precondition of case 1.

Once α_1, α_3, α_5 are obtained, all the intermediate parameters can be calculated. Then, the implicit dispersion equation for anti-symmetric modes defined in Eq. (22) can be generated, which is superficially a complex-valued equation with respect to ξ at $v_0 = 9000\,\mathrm{m/s}$ due to the existence of the complex exponential terms in matrix $\mathbf{D}_a(v,\xi)$. Thus, the standard solving procedures should handle both real and imaginary parts, represented in Eq. (23). We plot its function curves of real and imaginary parts in Fig. 2 to intuitively study the distribution of solutions of the equation $D_a(v_0 = 9000, \xi) = 0$ before solving it via bisection method.

Let us focus on the implicit curve firstly in both sub-figures of Fig. 2. For the real part, its curve is oscillating and chaotic, superficially indicating *'many spurious roots'* in the presented x-axis range. For the imaginary part, its curve is continuous and smooth and the seven zero-points can be clearly recognized as marked by red circles. Comparing the order of magnitude for both curves, the one of real part (10^{-8}) is largely smaller than the one of imaginary part (10^{7}).

Then, we superimpose the explicit curves to make deep comparison with the implicit curves, where the explicit curves are plotted based on the explicit expression, Eq. (28). In the sub-figure of imaginary part both curves are totally overlapped because the explicit expression just succeeds from the implicit one. In the sub-figure of real part the zero-valued explicit curve reflects the inference of Eq. (28) in a numerical way. As for the chaotic implicit curve, which should have been totally zero-valued in theory like the explicit curve, the reason lies in the numerical errors, e.g., round-off error or machine epsilon, that is inevitable when performing numerical analysis.

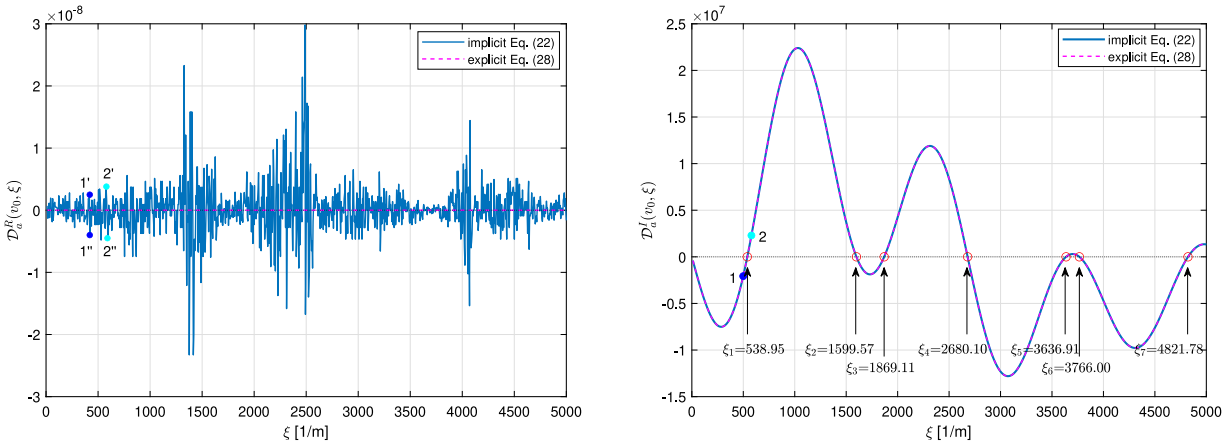

(a) real part $\mathcal{D}_a^R(v_0 = 9000, \xi)$ (b) imaginary part $\mathcal{D}_a^I(v_0 = 9000, \xi)$

Fig. 2. Using bisection method to solve the equation $D_a(v_0 = 9000, \xi) = 0$.

Anyway, the solving process should be focused on the effective part (imaginary part in this case). By sweeping ξ with a small enough step within an interested range, the accurate solutions of ξ can be solved via bisection method as shown in Fig. 2(b). These solutions correspond to the points of dispersion curves, v versus ξ, of the anti-symmetric modes at $v_0 = 9000\,\mathrm{m/s}$. The conventional dispersion curves v versus ω can be transformed from v versus ξ through $\omega = \xi v$.

One positive effect of dichotomy property is the ability to overcome the numerical instability issue encountered in [20], which adopts a phase change method[3] to solve the dispersion equation. In this paper, we exemplify the solution of $\xi_1 = 538.95$ to illustrate our improvement to the phase change method adapted to dichotomy property.

In the implicit curve of Fig. 2(b), there are two points 1 and 2 around the solution $\xi_1 = 538.95$. We map the two points on the complex plane as schematically shown in Fig. 3(a). It can be seen that each point may appear at any one of two positions in the complex plane due to the existence of tiny real part, see Fig. 2(a), caused by numerical error which can be regarded as a random disturbance to the theoretic positions locating on the y-axis in Fig. 3(a). In practice, no matter which $1'$ or $1''$ is identified, the phase angle of point 1 is approximately equal to $-90°$, and the phase angle of point 2 is approximately equal to $90°$. In Fig. 2(b), if moving point 1 to 2 along the curve, there should have a sudden $180°$ phase change in Fig. 3(a) when crossing the accurate solution $\xi_1 = 538.95$. Thus, like the bisection method, one can consecutively monitor the occurrence of $180°$ phase change to search ξ solutions.

Fig. 3(b) intuitively shows the continuous curves of phase angle changing with ξ. Employing the phase change method, all the ξ solutions can be obtained as shown in this figure, which are the same as the solutions via bisection method marked in Fig. 2(b).

Analysis of Case 2:

Adopting the previously introduced material properties and assigning a typical phase velocity $v_0 = 5000\,\mathrm{m/s}$ according to Table 1, the three predominant α solutions can be easily obtained as $\alpha_1 = 3.6014\mathrm{i}$, $\alpha_3 = 1.5933$, $\alpha_5 = 3.0868$. Apparently, only α_1 is a purely imaginary number, which is in agreement with the precondition of case 2. With the solved α_1, α_3, α_5, the implicit Eq. (22) and explicit Eq. (30) can be illustrated in Fig. 4, with the real and imaginary part respectively, to intuitively study the distribution of its solutions. As predicted in Eq. (30), for case 2, the real part becomes effective whereas due to the existence of numerical error the imaginary part becomes chaotic. Finally, the three solutions of ξ at $v_0 = 5000\,\mathrm{m/s}$ can be solved using bisection method as marked in Fig. 4(a).

In case 2, particular attention should be paid to the phase change method due to the existence of tiny imaginary part which will give rise to disorder in the phase angle. We take the solution of $\xi_2 = 3025.76$ as the example to illustrate this issue. Map the two points 1 and 2 in Fig. 4(a) on the complex plane as schematically shown in Fig. 5. Like in case 1, each point may appear at any one of two points in the complex plane due to the disturbance of tiny imaginary part. Thus, point $1'$ and $1''$ will be identified as two different phase angles respectively approaching to $180°$ and $-180°$, which will further give rise to oscillating in the phase angle curve as illustrated in Fig. 6(a). If directly applying phase change method to such an disordered curve, instability issue like spurious or loss roots will be faced [20]. Thus, when sweeping ξ to monitor phase change, the spurious phase angle of $-180°$ should be corrected as $180°$ firstly, as displayed in Fig. 6(b). Eventually, with the corrected phase angle curve, the ξ solutions can be obtained via phase change method as indicated in Fig. 6(b), which are the same as by using bisection method in Fig. 4(a).

[3] In the authors' opinion, the phase change method is evolved from the convergence criteria of *Disperse* that checks the included phase angle of the complex-valued dispersion function being greater than 90° for real solutions of dispersion equation [29].

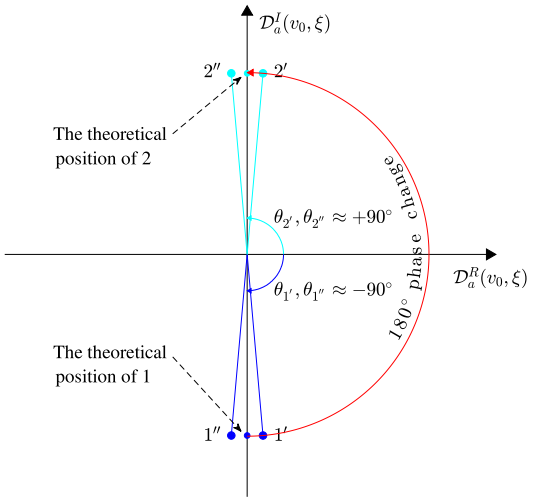

(a) schematic diagram of case 1

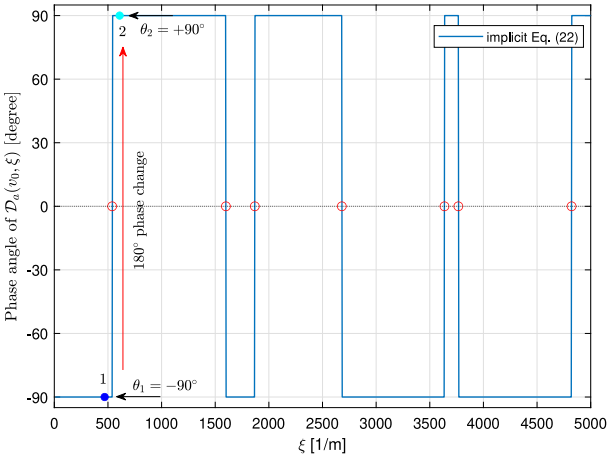

(b) phase curve of $\mathcal{D}_a(v_0=9000,\xi)$

Fig. 3. Using phase change method to solve the equation $\mathcal{D}_a(v_0=9000,\xi)=0$.

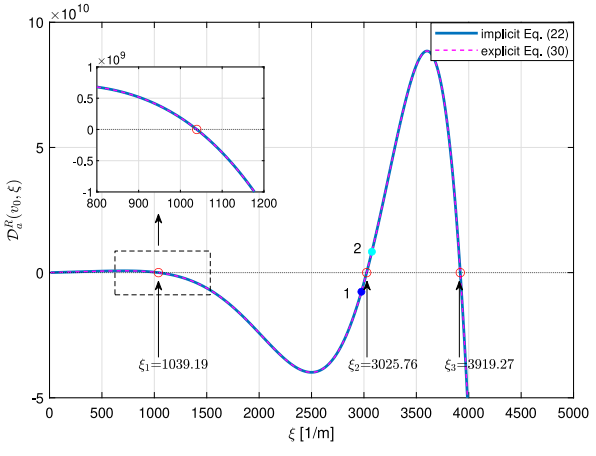

(a) real part $\mathcal{D}_a^R(v_0=5000,\xi)$

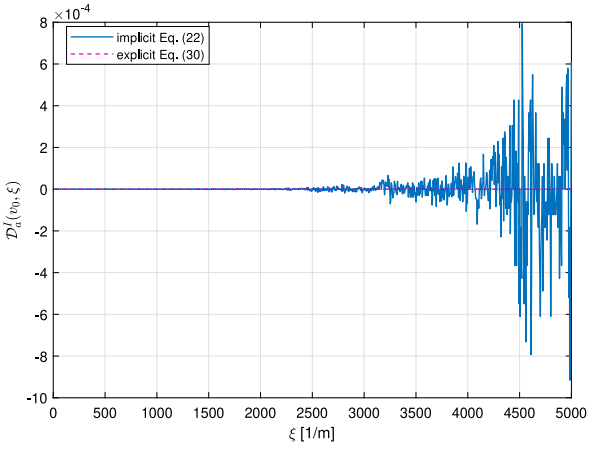

(b) imaginary part $\mathcal{D}_a^I(v_0=5000,\xi)$

Fig. 4. Using bisection method to solve the equation $\mathcal{D}_a(v_0=5000,\xi)=0$.

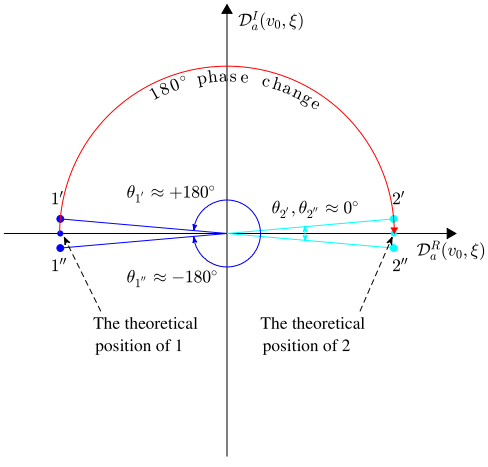

Fig. 5. The schematic diagram of phase change method for case 2.

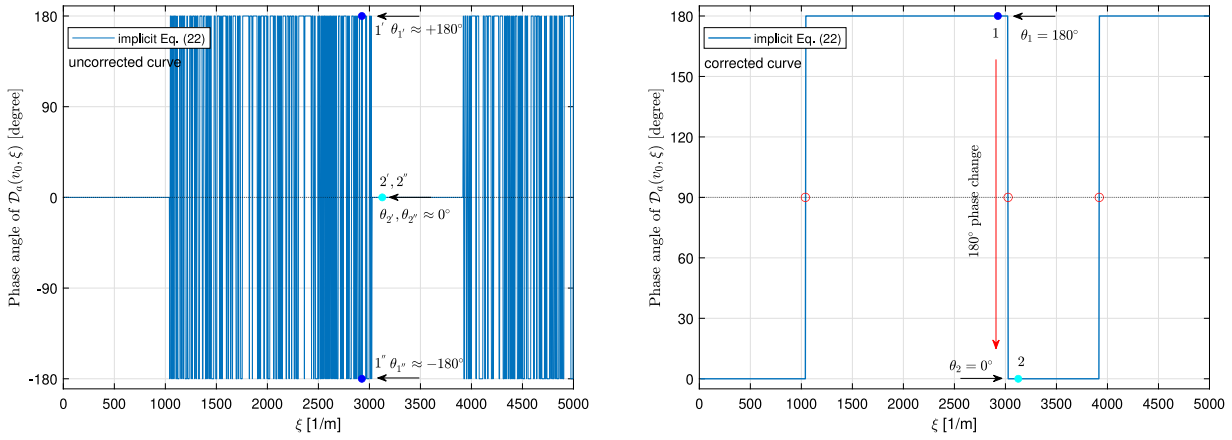

(a) uncorrected curve (b) corrected curve

Fig. 6. Using phase change method to solve the equation $D_a(v_0 = 5000, \xi) = 0$.

3.3. Dichotomy property of dispersion equation when sweeping v

The efforts made above are related with the dichotomy property when sweeping wavenumber ξ. Alternatively, this property is also owned when sweeping phase velocity v at a fixed ξ_0 but with more complexity, since at a fixed ξ_0, the process of sweeping v will cross all the four cases of α_1, α_3, α_5. However, when sweeping ξ, a single v_0 only leads to an unitary case among the four possible ones. Thanks to the theoretical derivations previously carried out, it is possible to automatically adapt when sweeping phase velocity. We only take here a numerical example to illustrate the solving process of the dispersion equation $D_a(v, \xi_0) = 0$ via both bisection and phase change methods which considers the dichotomy property when sweeping phase velocity.

It should be noted that the intermediate parameters, α_r, V_r, W_r, β_{ir} $(r = 1, 3, 5; i = 1, 2, 3)$ only depend on phase velocity v for the given material parameters. Thus, when sweeping ξ at a fixed v_0, all evaluations of $D_a(v_0, \xi)$ at all stagnation steps of ξ share the same intermediate parameters. However, when sweeping v at a fixed ξ_0, these intermediate parameters should be computed repeatedly at different stagnation steps of v, thus decelerating the sweeping speed. This point will be assessed in Section 6.2 by comparing the computational time of the two solving schemes.

Fig. 7 shows the typical function curves of implicit $D_a(v, \xi_0)$ at $\xi_0 = 1750\,[1/\mathrm{m}]$ in the format of real and imaginary parts as well as phase angle curves. It can be seen that the whole range of v interested is large enough to span all the four cases related with α_1, α_3, α_5. Within each case, only the effective part is plotted, and at the boundary of two different cases, there exists a switch between real and imaginary parts, this occurrence is accompanied by a 90° phase change in the phase angle curve. It should be noted that the phase angle curve in case 2 and 4 has been corrected in Fig. 7, and in case 3 there is no roots. In any case, the curves of real and imaginary parts should be fed to bisection method, or the corrected phase curve should be fed to phase change method, to get the solutions of v as indicated in Fig. 7.

After comprehensively studying the dichotomy property of dispersion equation for the anti-symmetric modes, we computed its complete dispersion curves as shown in Fig. 8(a), in which the horizontal and vertical dotted lines highlight the sweeping lines used in the previous paragraphs to exemplify the dichotomy property of different cases. The dichotomy property of symmetric modes, though not presented in this paper, can be also investigated by following the methodology used for anti-symmetric modes, thus its dispersion curves have been depicted in Fig. 8(b).

Comparing the two schemes of sweeping ξ and v from Fig. 8, sweeping ξ will lose many data points in a mode's non-dispersive ranges, like A0 mode in higher wavenumber, S0 mode in lower wavenumber and SH0 mode in the whole range of wavenumber. However, sweeping v will lose data points near to a mode's cutoff wavenumber, like A1 mode near to $500\,[1/\mathrm{m}]$. Therefore, in order to generate the complete dispersion curves, sweeping ξ and v simultaneously then combining both solution sets are necessary. In Ref. [20], an interpolation method is adopted to reconstruct the missing points in the discrete dispersion solutions. This is only valid for lower modes.

3.4. Dichotomy property of dispersion equation in $f - \xi$ and $f - v$ domains

The dispersion curves v versus ξ retrieved from the symmetry-ignored dispersion equation $D(v, \xi) = 0$ belong to actually the wavenumber–phase velocity domain. The conventional dispersion curves f versus ξ and v versus f can be retrieved from Eqs. (35a) and (35b), respectively, through the relation $f = \xi v/(2\pi)$.

$$\mathfrak{D}(f, \xi) \triangleq D(2\pi f/\xi, \xi) = 0 \quad \text{frequency–wavenumber domain} \tag{35a}$$

$$\mathfrak{d}(v, f) \triangleq D(v, 2\pi f/v) = 0 \quad \text{frequency–phase velocity domain} \tag{35b}$$

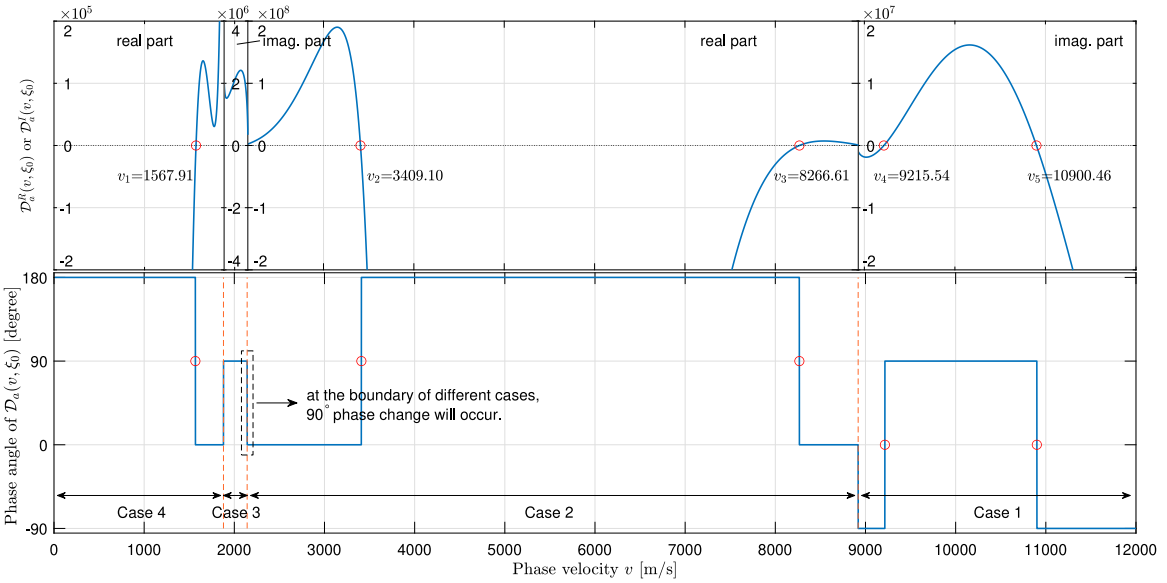

Fig. 7. Using bisection and phase change methods to solve the equation $D_a(v, \xi_0 = 1750) = 0$. The small width of case 3 is caused by the degree of anisotropy.

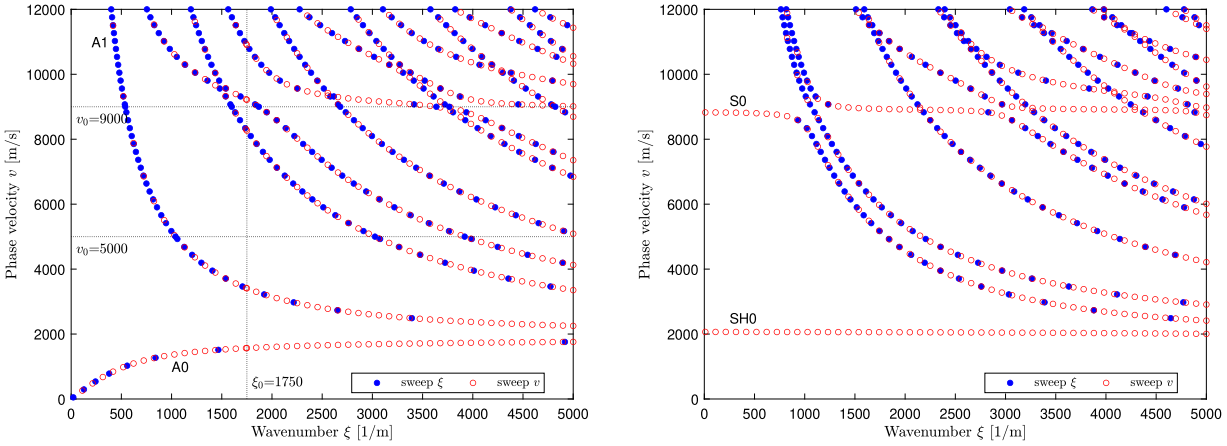

(a) anti-symmetric modes (b) symmetric modes

Fig. 8. Dispersion curves of the monoclinic lamina.

The newly generated two dispersion equations $\mathfrak{D}(f, \xi) = 0$ and $\mathfrak{d}(v, f) = 0$ still hold the dichotomy property because they naturally succeed from the equation $D(v, \xi) = 0$. Thus, bisection and phase change methods can be used to be the solver for the two equations, but the effective part should be identified firstly, and if the real part is the effective one, phase correction measure should be taken to avoid numerical instability issue.

4. Dispersion equation of guided waves in a laminate derived via GMM

The paradigm aforementioned concentrates on a single lamina. In this section, we will extend the dichotomy property of dispersion equation to a laminate as schematically shown in Fig. 1(b). For a multi-layered composite plate, there are generally three theoretical methods based on 3D elasticity to build its dispersion equation, TMM and its improved version SMM, as well as GMM. Here, we adopt GMM to study the dichotomy property of dispersion equation in a laminate due to its numerical stability and as well to avoid redundancy. The methodology used for GMM is still applicable to TMM and SMM. In the first place, the derivation process of GMM will be briefly introduced.

4.1. Global matrix method

For a typical layer l_k in Fig. 1(b), its displacement and stress fields follow the same expressions as a single lamina aforementioned. Hence, Eqs. (13) and (14) can be rewritten as the following matrix multiplication form in the context of a laminate.

$$\mathbf{u}^{l_k} = \boldsymbol{\Upsilon}^{l_k}\boldsymbol{\Lambda}^{l_k}(x_3)\boldsymbol{\eta}^{l_k}\mathrm{e}^{\mathrm{i}\xi(x_1-vt)} \tag{36a}$$

$$\boldsymbol{\sigma}^{l_k} = \boldsymbol{\beta}^{l_k}\boldsymbol{\Lambda}^{l_k}(x_3)\boldsymbol{\eta}^{l_k}\mathrm{e}^{\mathrm{i}\xi(x_1-vt)} \tag{36b}$$

where, the superscript 'l_k' denotes that the associated terms belong to a general layer l_k. $\boldsymbol{\Upsilon}^{l_k}$, $\boldsymbol{\beta}^{l_k}$, $\boldsymbol{\Lambda}^{l_k}(x_3)$ are defined as follows.

$$\boldsymbol{\Upsilon}^{l_k} = \begin{bmatrix} 1 & 1 & 1 & 1 & 1 & 1 \\ V_1 & V_2 & V_3 & V_4 & V_5 & V_6 \\ W_1 & W_2 & W_3 & W_4 & W_5 & W_6 \end{bmatrix}^{l_k}, \boldsymbol{\beta}^{l_k} = \begin{bmatrix} \beta_{11} & \beta_{12} & \beta_{13} & \beta_{14} & \beta_{15} & \beta_{16} \\ \beta_{21} & \beta_{22} & \beta_{23} & \beta_{24} & \beta_{25} & \beta_{26} \\ \beta_{31} & \beta_{32} & \beta_{33} & \beta_{34} & \beta_{35} & \beta_{36} \end{bmatrix}^{l_k},$$
$$\boldsymbol{\Lambda}^{l_k}(x_3) = \begin{bmatrix} \mathrm{e}^{\mathrm{i}\xi\alpha_1 x_3} & & \\ & \ddots & \\ & & \mathrm{e}^{\mathrm{i}\xi\alpha_6 x_3} \end{bmatrix}^{l_k} \tag{37}$$

It should be noted that when transferring Eq. (14) to Eq. (36b), the common factor $\mathrm{i}\xi$ has been suppressed since it has no effect on the continuity and boundary conditions to be evaluated subsequently. Eqs. (36a) and (36b) can be concatenated into a single equation.

$$\mathbf{S}^{l_k} = \boldsymbol{\Gamma}^{l_k}\boldsymbol{\Lambda}^{l_k}(x_3)\boldsymbol{\eta}^{l_k}\mathrm{e}^{\mathrm{i}\xi(x_1-vt)} = \mathbf{Z}^{l_k}(x_3)\boldsymbol{\eta}^{l_k}\mathrm{e}^{\mathrm{i}\xi(x_1-vt)} \tag{38}$$

where, $\mathbf{S}^{l_k} = \left[\mathbf{u}^{l_k\mathrm{T}}, \boldsymbol{\sigma}^{l_k\mathrm{T}}\right]^{\mathrm{T}}$ is the field variables. $\mathbf{Z}^{l_k}(x_3) = \boldsymbol{\Gamma}^{l_k}\boldsymbol{\Lambda}^{l_k}(x_3)$ and $\boldsymbol{\Gamma}^{l_k} = \left[\boldsymbol{\Upsilon}^{l_k\mathrm{T}}, \boldsymbol{\beta}^{l_k\mathrm{T}}\right]^{\mathrm{T}}$.

In a laminate, we have the CC at all interfaces of two adjacent layers and traction free BC at the top and bottom surfaces of the laminate. Specifically, at a typical interface i_k as illustrated in Fig. 1(b), the field variables of layer l_k at its bottom side should equal to the field variables of layer l_{k+1} at its top side as a result of rigid connection.

$$\mathbf{S}^{l_k}_{\mathrm{bot}} = \mathbf{S}^{l_{k+1}}_{\mathrm{top}} \quad (k = 1, \ldots, n-1) \tag{39}$$

where, the subscript 'bot' and 'top' represents bottom and top side, respectively.

Substituting Eq. (38) into Eq. (39) can lead to the following equation.

$$\mathbf{Z}^{l_k}_{\mathrm{bot}}\boldsymbol{\eta}^{l_k} - \mathbf{Z}^{l_{k+1}}_{\mathrm{top}}\boldsymbol{\eta}^{l_{k+1}} = \mathbf{0} \quad (k = 1, \ldots, n-1) \tag{40}$$

where, $\mathbf{Z}^{l_k}_{\mathrm{bot}} = \mathbf{Z}^{l_k}(d_k) \in \mathbb{C}^{6\times6}$, $\mathbf{Z}^{l_{k+1}}_{\mathrm{top}} = \mathbf{Z}^{l_{k+1}}(0) \in \mathbb{C}^{6\times6}$.

For the traction free BC at the top- and bottom-most surfaces as shown in Fig. 1(b), it corresponds to the following equation.

$$\boldsymbol{\sigma}^{l_1}_{\mathrm{top}} = \mathbf{0} \quad \text{and} \quad \boldsymbol{\sigma}^{l_n}_{\mathrm{bot}} = \mathbf{0} \tag{41}$$

Substituting Eq. (36b) into Eq. (41) can lead to Eq. (42).

$$\mathbf{Z}^{\sigma,l_1}_{\mathrm{top}}\boldsymbol{\eta}^{l_1} = \mathbf{0} \quad \text{and} \quad \mathbf{Z}^{\sigma,l_n}_{\mathrm{bot}}\boldsymbol{\eta}^{l_n} = \mathbf{0} \tag{42}$$

where, $\mathbf{Z}^{\sigma,l_1}_{\mathrm{top}} = \boldsymbol{\beta}^{l_1}\boldsymbol{\Lambda}^{l_1}(0) \in \mathbb{C}^{3\times6}$, $\mathbf{Z}^{\sigma,l_n}_{\mathrm{bot}} = \boldsymbol{\beta}^{l_n}\boldsymbol{\Lambda}^{l_n}(d_n) \in \mathbb{C}^{3\times6}$.

Sequentially applying Eq. (40) from interface i_1 to i_{n-1} as illustrated in Fig. 1(b) and combining Eq. (42), all the resulted equations can be regularly organized to a global linear homogeneous equation set, Eq. (43), which requires the vanished determinant of the coefficients matrix, $\mathbf{D}_G(v,\xi) \in \mathbb{C}^{6n\times6n}$, finally generating the implicit dispersion equation of guided waves propagating in a laminate as presented in Eq. (44).

$$\begin{matrix} \text{BC at the top surface} \rightarrow \\ \text{CC at the interfaces} \\ \text{BC at the bot. surface} \rightarrow \end{matrix} \left\{ \begin{bmatrix} -\mathbf{Z}^{\sigma,l_1}_{\mathrm{top}} & & & \\ \mathbf{Z}^{l_1}_{\mathrm{bot}} & -\mathbf{Z}^{l_2}_{\mathrm{top}} & & \\ \ddots & \ddots & & \\ & \mathbf{Z}^{l_k}_{\mathrm{bot}} & -\mathbf{Z}^{l_{k+1}}_{\mathrm{top}} & \\ & \ddots & \ddots & \\ & & \mathbf{Z}^{l_{n-1}}_{\mathrm{bot}} & -\mathbf{Z}^{l_n}_{\mathrm{top}} \\ & & & \mathbf{Z}^{\sigma,l_n}_{\mathrm{bot}} \end{bmatrix} \begin{bmatrix} \boldsymbol{\eta}^{l_1} \\ \vdots \\ \boldsymbol{\eta}^{l_k} \\ \vdots \\ \boldsymbol{\eta}^{l_n} \end{bmatrix} = \mathbf{0} \right. \tag{43}$$

$$\mathcal{D}_G(v,\xi) \triangleq \det\{\mathbf{D}_G(v,\xi)\} = 0 \tag{44}$$

where, the subscript 'G' denotes that the dispersion equation is built with GMM.

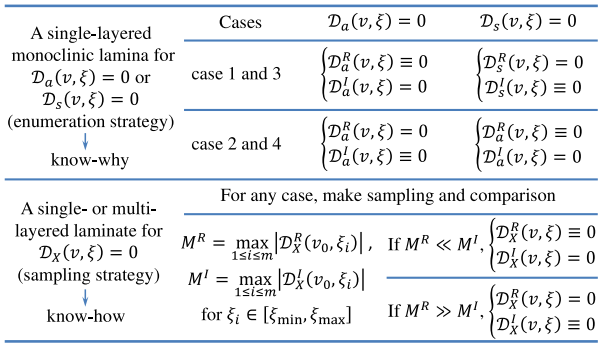

X represents a or s for a single-layered monoclinic lamina, or G, T, S for a multi-layered laminate respectively representative of GMM, TMM, SMM.

(a)

	Effective part	Bisection method	Phase change method
Sweep ξ at $v=v_0$	$\mathcal{D}_X^I(v_0,\xi)=0$	★★(1)	★★(1)
	$\mathcal{D}_X^R(v_0,\xi)=0$	★★(1)	★★(1,3)
Sweep v at $\xi=\xi_0$	$\mathcal{D}_X^I(v,\xi_0)=0$	★(2)	★(2)
	$\mathcal{D}_X^R(v,\xi_0)=0$	★(2)	★(2,3)

Comments on the numerical labels:

(1) The intermediate parameters keep constants for a fixed v_0, which maximizes the computational efficiency of both methods.

(2) The intermediate parameters are computed repeatedly for different v, which slows down the computational efficiency of both methods.

(3) Phase correction measure should be taken to avoid numerical instability.

(b)

Fig. 9. Concluding figures: (a) the strategy to determine the dichotomy property of dispersion equation, (b) the computational efficiency of solving methods adapted to dichotomy property.

4.2. Dichotomy property of dispersion equation derived via GMM

It is clear that $\mathbf{D}_G(v,\xi)$ in Eq. (43) is a complex-valued matrix, thus superficially its determinant $\mathcal{D}_G(v,\xi)$ should be a complex-valued function having real, $\mathcal{D}_G^R(v,\xi)$, and imaginary, $\mathcal{D}_G^I(v,\xi)$, parts simultaneously. However, like in the context of a single monoclinic lamina, we have also observed the dichotomy property of $\mathcal{D}_G(v,\xi)$, that is to say, in some ranges of v the real part is identically vanishing, $\mathcal{D}_G^R(v_0,\xi)\equiv 0$, while in other ranges of v, $\mathcal{D}_G^I(v_0,\xi)\equiv 0$. Strictly proving this property for an arbitrary n-layered laminate is not reachable since the explicit expression of $\mathcal{D}_G(v,\xi)$ is no longer available. Furthermore, in extreme conditions, the total number of cases in a general n-layered laminate will be as large as $3n+1$ given that each layer has three critical velocities according to Eq. (27) such that the case by case deduction is no more realizable.

In order not to stuck in intractable mathematical pitfall, we propose a sampling strategy to investigate the dichotomy property of dispersion equation in a numerical way through making qualitative analysis. Inspired by the investigation on the single monoclinic lamina, the dichotomy property of dispersion equation in the context of laminate stems from the property of the intermediate parameters of each layer, which is actually controlled by the common phase velocity v once each layer's material properties are given. Thus, no matter what value the fixed v_0 is, the implicit function $\mathcal{D}_G(v_0,\xi)$ defined in Eq. (44) with ξ being the argument can be divided into real part $\mathcal{D}_G^R(v_0,\xi)$ and imaginary part $\mathcal{D}_G^I(v_0,\xi)$, no matter which part being the vanished one, it will not be totally zero in practice due to numerical error. However, we can uniformly sample m points for the two functions within the interested range $[\xi_{\min},\xi_{\max}]$, and find the maximum absolute function value from these sampling points for each part.

$$M^R=\max_{1\le i\le m}|\mathcal{D}_G^R(v_0,\xi_i)|,\quad M^I=\max_{1\le i\le m}|\mathcal{D}_G^I(v_0,\xi_i)|\quad \text{for } \xi_i\in[\xi_{\min},\xi_{\max}] \tag{45}$$

Finally, the dichotomy property is determined by comparing the true maximum values between the two parts, meanwhile, the effective part can be obtained by using the following rule.

- If $M^R\gg M^I$, the effective part is $\mathcal{D}_G^R(v_0,\xi)$ and $\mathcal{D}_G^I(v_0,\xi)\equiv 0$;
- If $M^R\ll M^I$, the effective part is $\mathcal{D}_G^I(v_0,\xi)$ and $\mathcal{D}_G^R(v_0,\xi)\equiv 0$.

The sampling strategy is achievable due to the fact that the vanished part, though polluted by numerical error, is lower than the effective part by several orders of magnitude. Furthermore, this sampling strategy is very easy to implement and it is also an universal strategy to determine the dichotomy property of dispersion equation not only applicable for GMM but also for TMM, SMM and the single lamina (for both cases $\Delta\le 0$ and $\Delta>0$) as concluded in Fig. 9(a). In this figure, using the enumeration strategy to determine the dichotomy property of a single-layered plate reflects the know-why of this property, and adopting the sampling strategy embodies the know-how to characterize this property for a complex structure in practice.

With the deterministic dichotomy property for any case, the dispersion equation can be solved by sweeping ξ at a fixed v_0 or sweeping v at a fixed ξ_0 via bisection or phase change methods, as summarized in Fig. 9(b), in which two stars represent a higher computational efficiency than one star. This subfigure is also validated in Section 6.2.

5. Overcoming common numerical issues using dichotomy property

After studying the dichotomy property, some numerical issues frequently reported in literature can be overcome with the help of dichotomy property. Two typical issues are the instability of the phase change method and the instability of TMM.

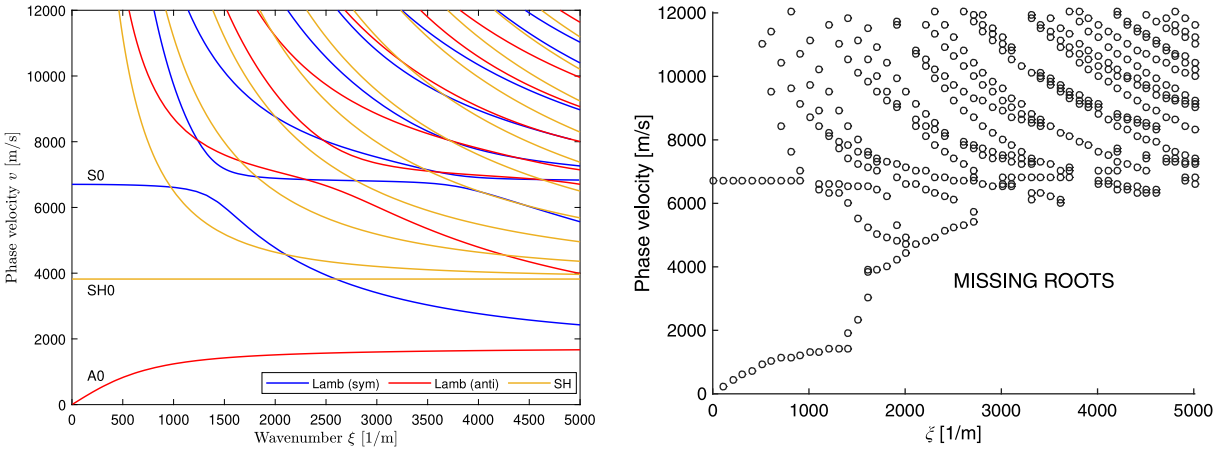

(a) recomputed graph via GMM and CPCM (b) graph showing numerical instabilities (from [20])

Fig. 10. Dispersion curves propagating at 0° for the $[0]_{50}$ orthotropic laminate.

5.1. Overcoming numerical instability of the phase change method

In [20] numerical instabilities were encountered when generating the dispersion curves of a 50-layered orthotropic laminate via GMM, see Fig. 10(b). This laminate has a special layup $[0]_{50}$, i.e., each layer orients at the same fiber direction. The authors of [20] alleged that the numerical instabilities were caused by the large number of layers under study, and the maximum ability of their method to compute a laminate must be no more than 13 layers in order to obtain satisfying results for GMM.

In this section, we recompute the dispersion curves of this laminate by using the same GMM and corrected phase change method (CPCM), as shown in Fig. 10(a) (the material properties used is listed in Appendix D and the absence of $\Delta > 0$ for this material has been checked.). It can be seen that our results do not suffer from instability issue anymore. The reason is that when solving dispersion equation built with GMM via phase change method, at the region of missing roots in Fig. 10(b), phase correction measure should be taken. However in Ref. [20], the direct phase change method was employed thus suffering of numerical instability issue is inevitable.

5.2. Overcoming numerical instability of TMM

TMM usually suffers from instability issue known as the so-called "*large fd problem*" which refers to the unstable solutions at a large product value of frequency f and plate thickness d. One typical example citing from [27] is plotted on Fig. 11(b) for illustration, in the frequency–wavenumber domain. In this graph, the red curve divides the graph into two parts, with the left part of solutions via TMM and right part via SMM, because either method suffered from instability in its opposite part as explained in [27]. Note that Fig. 11(b) corresponds to a single-layered unidirectional composite plate at 45° direction, and the material properties of this plate is given in Appendix D.

Before generating the final dispersion curves using our method, we checked firstly the presence of $\Delta > 0$ by making the curve of Δ with respect to v as shown in Fig. 12(a), as long as substituting the given material parameters into Eqs. (9) and (A.1). Fig. 12(a) shows the presence of $\Delta > 0$ when $v \in (0, v_\Delta)$ where $v_\Delta = 1648.05$ such that $\Delta(v_\Delta) = 0$. For this special case, there is a need to explore whether or not the dichotomy property still holds. Nonetheless, the complexity of this case hinders the theoretical manner on dichotomy property that is used in the enumeration strategy. Thus, making numerical validation is the sensible way. For this purpose, we arbitrarily assign $v_0 = 1000$ that consequently leads to $\Delta = 24.05$ and $\alpha_1^2 = -11.89$, $\alpha_3^2 = -0.69 - 0.20\mathrm{i}$, $\alpha_5^2 = -0.69 + 0.20\mathrm{i}$. Clearly, α_1^2 is a real number and α_3^2 and α_5^2 are mutually complex-conjugated. Then, the function curve of $\mathcal{D}_a(v_0 = 1000, \xi)$ can be generated in Fig. 12(b) as real and imaginary part, respectively. This sub-figure clearly shows the preservation of dichotomy property in the special case $\Delta > 0$, with the real part effective that is identified automatically through the sampling strategy formalized in Eq. (45).

In order to match the frequency–wavenumber domain in Fig. 11(b), we take advantage of the same domain dispersion equation, Eq. (35a), to retrieve the dispersion curves of the single-layered unidirectional composite plate as delineated in Fig. 11(a) lying in the right part being the propagating waves, which is achieved via bisection method through sweeping f at a series of fixed ξ_0 or sweeping ξ at a series of fixed f_0. It can be seen that the instability issue does not occur in our computation, thus proving the stability and robustness of our method that accounts for the dichotomy property.

What needs to be clarified is that the terminology *'propagating waves'* in Fig. 11(a) means that the waves can persistently propagate in the plate without energy loss, in contrast to it, the counterpart *'evanescent waves'* refers to the heavily attenuated waves since the energy of this kind of waves is quickly dissipated, as a result, its range of propagation is limited to the near field of

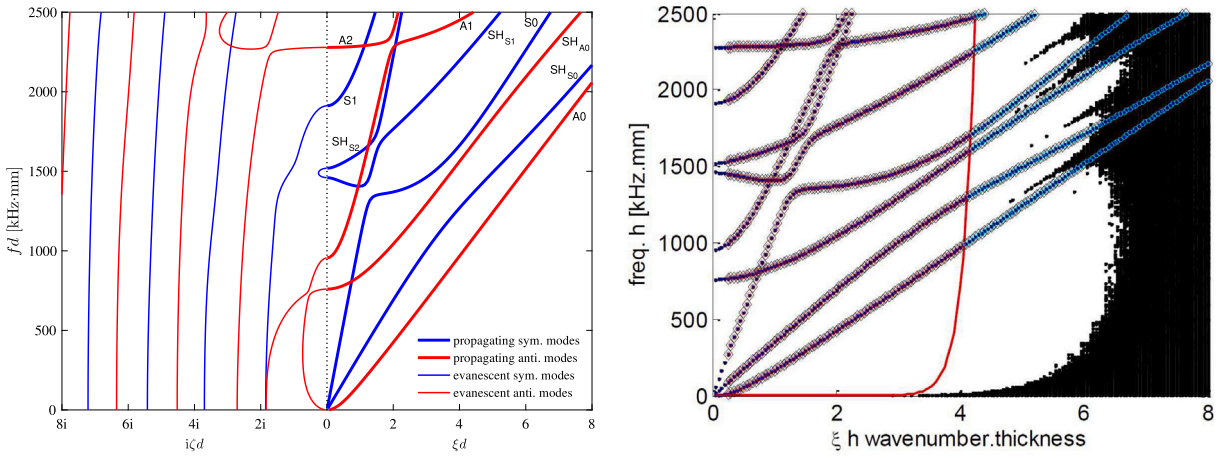

(a) evanescent (iζd) and propagating (ξd) waves (b) graph showing instability of TMM (from [27])

Fig. 11. Dispersion curves in frequency–wavenumber domain propagating at 45° of the single-layered unidirectional composite plate.

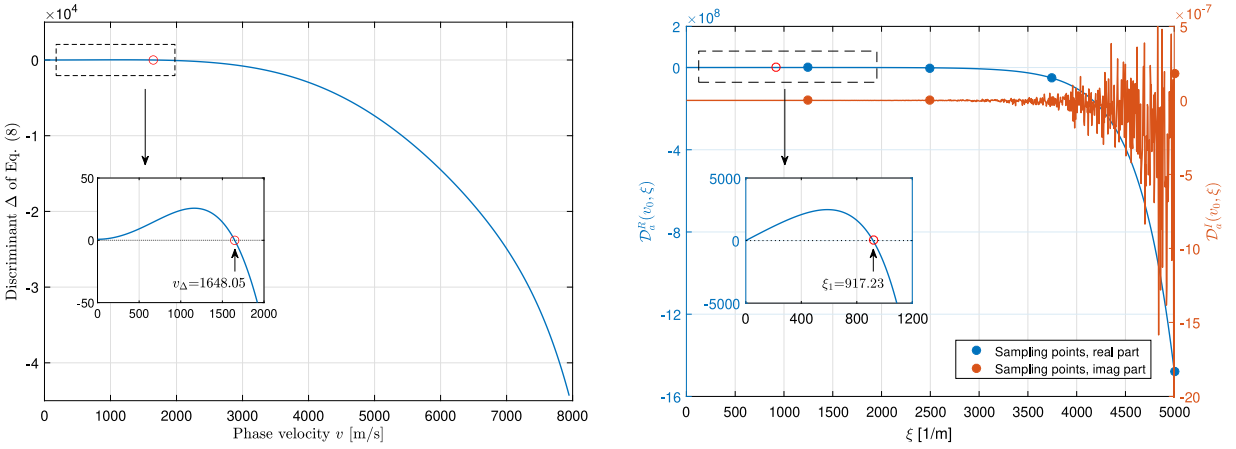

(a) curve of Δ with respect to v (b) curve of $\mathcal{D}_a(v_0 = 1000, \xi)$

Fig. 12. Dichotomy property of dispersion equation at $v_0 = 1000\,\mathrm{m/s}$ that invokes $\Delta > 0$.

the source. The evanescent waves have received increasing attention in the recent years [36,37], but both references only focused on isotropic materials by working out the conventional Rayleigh–Lamb dispersion equation instead of composites, in terms of theoretical analysis, thanks to the complexity of the evanescent waves propagating in composite plate. In the following paragraph, we describe how to analytically obtain the dispersion curves of the evanescent waves propagating in the single-layered composite plate, as shown in Fig. 11(a).

In the mathematical formulation, both the propagating and evanescent waves are the solutions of the dispersion equation, respectively representing the real-valued wavenumber ξ and the purely imaginary-valued wavenumber iζ wherein ζ is a real number. The dispersion equation regarding to the evanescent waves can be formed by substituting $\xi = \mathrm{i}\zeta$ into Eq. (24a) or (24b) to generate $D(v, \mathrm{i}\zeta) = 0$, ignoring the symmetry. In Appendix C, we have proved that $D(v, \mathrm{i}\zeta)$ still holds the dichotomy property. For the dispersion equation in frequency–wavenumber domain, we further substitute $\xi = \mathrm{i}\zeta$ into Eq. (35a) to generate $\mathfrak{D}(f, \mathrm{i}\zeta) = 0$, whose dichotomy property can be theoretically or numerically proved but not presented in this paper for brevity.

With the closed-form dispersion equation of the evanescent waves in frequency–wavenumber domain, the dispersion curves can be obtained by solving the effective part through sweeping f at a series of fixed ζ_0 or sweeping ζ at a series of fixed f_0, by virtue of bisection or phase change method, as illustrated in Fig. 11(a) lying in the left part being the evanescent waves. It can be seen that the evanescent waves connect with the propagating waves at zero wavenumber. Furthermore, some evanescent modes connect two different propagating modes possessing the same symmetry. For example, the first anti-symmetric evanescent mode connects the propagating A0 and $\mathrm{SH}_{\mathrm{A0}}$ modes, and the first symmetric evanescent mode connect the propagating $\mathrm{SH}_{\mathrm{S1}}$ and $\mathrm{SH}_{\mathrm{S2}}$ modes. This phenomenon has also been observed in [37] but via semi-analytical finite element (SAFE) method for most of non-isotropic

Table 2
The computational time of the 50-layered plate (unit: seconds).

Bisection method			Phase change method		
Sweep v	Sweep ξ	Sum	Sweep v	Sweep ξ	Sum
6437[s]	3052[s]	9489[s]	6729[s]	3071[s]	9800[s]
2284[p]	1058[p]	3342[p]	2338[p]	1052[p]	3390[p]

[s]Serial computing technique is applied.
[p]Parallel computing technique is applied.

materials. Our theoretical analysis on the unidirectional composite plate contribute a plus to the theory of guided waves propagation in composite materials.

Finally, the emphasis should be placed on the multi-layered composite laminate in terms of the dispersion equation of the evanescent waves built by GMM, which possesses the dichotomy property as well. Thus, as the analysis for propagating waves in a laminate, the sampling strategy should be a simple and efficient tool to retrieve the dispersion curves of the evanescent waves.

6. Discussion

6.1. Parallelization of GMM

Even if not so apparent, GMM can be perfectly parallelized. One can observe Fig. 8 to obviously assess that the two sweeping schemes, i.e., sweeping ξ and sweeping v, are mutually independent. Moreover, in both sweeping scheme, the sweeping process between the different fixed variables is mutually independent as well. For the example of sweeping ξ, the two equations $D(v_0^{(1)}, \xi) = 0$ and $D(v_0^{(2)}, \xi) = 0$ can be solved concurrently as there is no any communication between the two equations. It is also true when sweeping v, the two equations $D(v, \xi_0^{(1)}) = 0$ and $D(v, \xi_0^{(2)}) = 0$ can be solved concurrently. This fact indicates that the two sweeping processes belongs to the classical *Perfectly Parallel Problem* [38]. Thus, execution of GMM can be parallelized during programming the algorithm to intentionally cope with the computational efficiency issue. Applying the parallel computing techniques for GMM can be easily achieved since there are many numerical computing toolboxes or packages available from the widely used programming languages such as Matlab and Python.

6.2. Comparison of computational efficiencies

In this section, we compare the computational efficiencies of the two solving methods (bisection and phase change methods) for the serial and parallel computing techniques by using the 50-layered plate in Section 5.1. Computations were performed in MATLAB R2016a hosted on a Dell Precision T3500 workstation with the processor Intel Xeon W3530@2.8 GHz, 4 CPU cores, 18G RAM. Computing range is shown in Fig. 10. Bi-directional sweeping scheme is used. In each direction, the sweeping line is equally offsetted 100 times from the minimum to the maximum, and the precision of solutions is set to be the fifth decimal place. The sweeping step length of phase velocity and wavenumber is 10 m/s and 10 [1/m], respectively. Each solving method runs 10 times and the averaged computational time is listed in Table 2.

Table 2 shows that sweeping v costs more time than sweeping ξ irrespective of the serial or parallel computing technique. The explanations to them are given in Section 3.3. Additionally, the speed-up ratio of the computational time between parallel and serial computing technique is as large as 2.8 for a computer with four CPU cores, which is desired. Finally, the computational time of CPCM is slightly greater than the counterpart of bisection method, which is due to the phase correction operation. The comparison result of Table 2 validates Fig. 9(b).

6.3. Generalization of dichotomy property in other material classes

The methodology developed in this paper can be also applied to other material classes like triclinic material, which is full anisotropy having 21 independent elastic coefficients, and piezoelectric material, whose dispersion equations are more complex than composite materials. After investigation for a certain material, if dichotomy property does not present in it, both the real and imaginary parts of dispersion function are effective in this case such that the true roots of the dispersion equation are the intersected roots of real and imaginary parts, i.e., Eq. (23) should be applied. An example of this case for a triclinic material,[4] whose parameters are provided in Appendix D, is illustrated in Fig. 13(a). However, for this case, phase change method is still applicable without need to take phase correction measure because phase angle changes smoothly with searching variable as illustrated in Fig. 13(b).

[4] The dispersion equations of a triclinic material are not presented in this paper for the sake of brevity, but can be partly referred from [34].

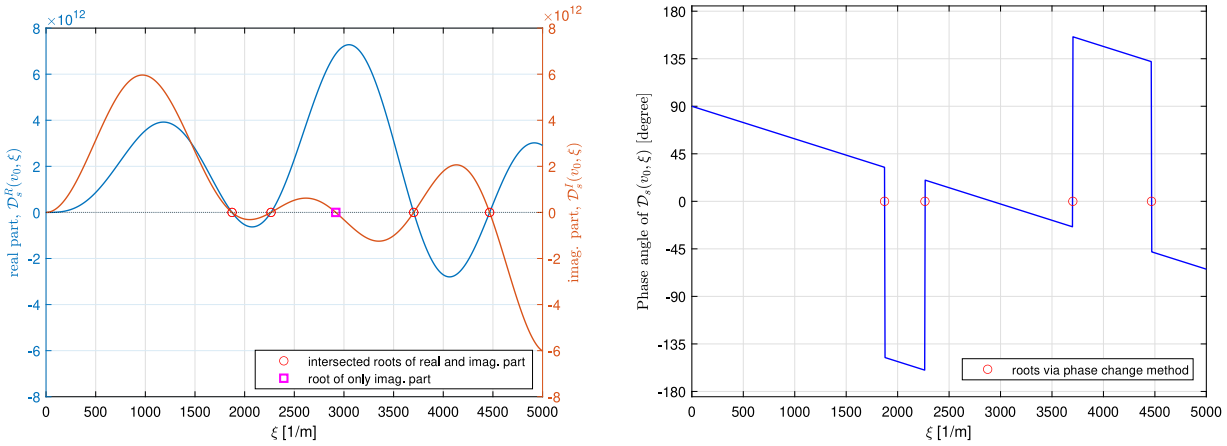

(a) real and imag. part curve of $\mathcal{D}_s(v_0,\xi)$ (b) phase angle curve of $\mathcal{D}_s(v_0,\xi)$

Fig. 13. Function curve of the symmetric modes of dispersion equation $D_s(v_0,\xi)$ for a triclinic material at $v_0 = 4000\,\mathrm{m/s}$.

7. Conclusions

The dispersion equation of guided waves propagating in composite plates are not a completely complex-valued equation, and it presents the dichotomy property of being either a real- or purely imaginary-valued equation. This property is strictly investigated firstly for a single-layered monoclinic lamina in the case $\Delta \leq 0$ by using the enumeration strategy, showing that there exists four cases for α_1, α_3, α_5 depending on their properties of being real or purely imaginary number. The three parameters will lead to two mutually-exclusive effective parts, real and imaginary parts of the dispersion equation. Bisection and phase change methods are two efficient ways to solve the dispersion equations, but if the real part becomes to be effective one, phase correction measure should be taken toward to the phase change method in order to overcome some numerical instability issues.

The dichotomy property is further extended to a general multi-layered composite laminate through the proposed sampling strategy under the framework of GMM, but it is still applicable to TMM and SMM. The enumeration strategy and sampling strategy reflect the know-why and know-how aspects of the dichotomy property, respectively. Although this paper comprehensively studies the dichotomy property of dispersion equation in wavenumber–phase velocity domain, the counterparts in frequency–wavenumber and frequency–phase velocity domain still hold this property, as well as in the case of evanescent wave modes. Thus, this property has formed a closure characteristic on itself in mathematical sense as long as the damping effect is not involved.

A parallel computing technique is developed to improve the computational efficiency of the traditional GMM. With such, the proposed methodology has the potential to become a standard method to solve the damping free dispersion equations with stable, multipurpose and numerically efficient ways.

CRediT authorship contribution statement

Shuanglin Guo: Methodology, Software, Investigation, Writing – original draft. **Marc Rebillat:** Methodology, Writing – original draft, Visualization, Supervision, Validation. **Nazih Mechbal:** Conceptualization, Validation, Writing – review & editing, Supervision, Project administration, Funding acquisition.

Declaration of competing interest

The authors declare that they have no known competing financial interests or personal relationships that could have appeared to influence the work reported in this paper.

Acknowledgments

The first author appreciates the financial support from the China Scholarship Council (CSC). The authors are grateful for the anonymous reviewers whose valuable comments greatly improve the quality of this paper.

Appendix A. The polynomial coefficients about α^2

$$
\begin{aligned}
A_6 &= C_{33}C_{44}C_{55} - C_{33}C_{45}^2 \\
A_4 &= (C_{44}C_{55} - C_{45}^2)(C_{55} - \rho v^2) + C_{33}C_{55}(C_{66} - \rho v^2) + C_{33}C_{44}(C_{11} - \rho v^2) \\
&\quad - 2C_{16}C_{45}C_{33} + 2(C_{36} + C_{45})(C_{13} + C_{55})C_{45} \\
&\quad - (C_{13} + C_{55})^2 C_{44} - (C_{45} + C_{36})^2 C_{55} \\
A_2 &= C_{33}(C_{11} - \rho v^2)(C_{66} - \rho v^2) + C_{44}(C_{11} - \rho v^2)(C_{55} - \rho v^2) \\
&\quad + C_{55}(C_{66} - \rho v^2)(C_{55} - \rho v^2) - (C_{11} - \rho v^2)(C_{45} + C_{36})^2 \\
&\quad - (C_{66} - \rho v^2)(C_{13} + C_{55})^2 - 2(C_{55} - \rho v^2)C_{16}C_{45} \\
&\quad + 2C_{16}(C_{45} + C_{36})(C_{13} + C_{55}) - C_{16}^2 C_{33} \\
A_0 &= \left[(C_{11} - \rho v^2)(C_{66} - \rho v^2) - C_{16}^2\right](C_{55} - \rho v^2)
\end{aligned}
\tag{A.1}
$$

Appendix B. Proof of the properties of the intermediate parameters in Section 3.1

Property 1 is trivial. One just needs to check Eq. (11) for calculating V_r, W_r and Eq. (15) for calculating β_{1r}, β_{2r}, β_{3r}, meanwhile keep in mind that all the algebraic manipulations in Eqs. (11) and (15) only involving in real numbers if α_r is a real number.

For the Property 2, set $\alpha_r = \mathrm{i}a_r$, here a_r is a real number, and substitute it into Eq. (11) to make the following derivations.

$$
\begin{aligned}
V_r &= \frac{K_{11}(\mathrm{i}a_r)K_{23}(\mathrm{i}a_r) - K_{12}(\mathrm{i}a_r)K_{13}(\mathrm{i}a_r)}{K_{13}(\mathrm{i}a_r)K_{22}(\mathrm{i}a_r) - K_{12}(\mathrm{i}a_r)K_{23}(\mathrm{i}a_r)} \\
&= \frac{(C_{11} - \rho v^2 - C_{55}a_r^2)(C_{36} + C_{45})\mathrm{i}a_r - (C_{16} - C_{45}a_r^2)(C_{13} + C_{55})\mathrm{i}a_r}{(C_{13} + C_{55})\mathrm{i}a_r(C_{66} - \rho v^2 - C_{44}a_r^2) - (C_{16} - C_{45}a_r^2)(C_{36} + C_{45})\mathrm{i}a_r} \\
&= \frac{(C_{11} - \rho v^2 - C_{55}a_r^2)(C_{36} + C_{45}) - (C_{16} - C_{45}a_r^2)(C_{13} + C_{55})}{(C_{13} + C_{55})(C_{66} - \rho v^2 - C_{44}a_r^2) - (C_{16} - C_{45}a_r^2)(C_{36} + C_{45})} \\
&\Rightarrow \text{a real number}
\end{aligned}
$$

$$
\begin{aligned}
W_r &= \frac{K_{11}(\mathrm{i}a_r)K_{23}(\mathrm{i}a_r) - K_{12}(\mathrm{i}a_r)K_{13}(\mathrm{i}a_r)}{K_{12}(\mathrm{i}a_r)K_{33}(\mathrm{i}a_r) - K_{13}(\mathrm{i}a_r)K_{23}(\mathrm{i}a_r)} \\
&= \frac{(C_{11} - \rho v^2 - C_{55}a_r^2)(C_{36} + C_{45})\mathrm{i}a_r - (C_{16} - C_{45}a_r^2)(C_{13} + C_{55})\mathrm{i}a_r}{(C_{16} - C_{45}a_r^2)(C_{55} - \rho v^2 - C_{33}a_r^2) - (C_{13} + C_{55})\mathrm{i}a_r(C_{36} + C_{45})\mathrm{i}a_r} \\
&= \mathrm{i}\frac{(C_{11} - \rho v^2 - C_{55}a_r^2)(C_{36} + C_{45})a_r - (C_{16} - C_{45}a_r^2)(C_{13} + C_{55})a_r}{(C_{16} - C_{45}a_r^2)(C_{55} - \rho v^2 - C_{33}a_r^2) + (C_{13} + C_{55})(C_{36} + C_{45})a_r^2} \\
&\Rightarrow \text{a purely imaginary number}
\end{aligned}
$$

In this case, set $W_r = \mathrm{i}w_r$, here w_r is a real number, but keep V_r unchanged because it is already a real number. Substitute $\mathrm{i}a_r$, V_r, $\mathrm{i}w_r$ into Eq. (15) to make further derivations.

$$
\begin{aligned}
&\beta_{1r} = C_{13} + C_{36}V_r + C_{33}(\mathrm{i}a_r)(\mathrm{i}w_r) = C_{13} + C_{36}V_r - C_{33}a_r w_r \Rightarrow \text{a real number} \\
&\beta_{2r} = C_{45}(\mathrm{i}a_r) + C_{44}(\mathrm{i}a_r)V_r + C_{45}(\mathrm{i}w_r) = \mathrm{i}(C_{45}a_r + C_{44}a_r V_r + C_{45}w_r) \Rightarrow \text{an imag. number} \\
&\beta_{3r} = C_{55}(\mathrm{i}a_r) + C_{45}(\mathrm{i}a_r)V_r + C_{55}(\mathrm{i}w_r) = \mathrm{i}(C_{55}a_r + C_{45}a_r V_r + C_{55}w_r) \Rightarrow \text{an imag. number}
\end{aligned}
$$

For the Property 3, according to the Property 1 and 2, no matter what α_r being a real or purely imaginary number, V_r, β_{1r} are always real numbers for $r = 1, 3, 5$. Thus, B_5 defined in Eq. (25) is always a purely imaginary number because of

$$
B_5 = 8\mathrm{i}\left[V_1(\beta_{15} - \beta_{13}) + V_3(\beta_{11} - \beta_{15}) + V_5(\beta_{13} - \beta_{11})\right] = \mathrm{i}P_5 \Rightarrow \text{an imag. number}
$$

where, P_5 is definitely a real number.

Appendix C. Dichotomy property of the evanescent waves propagating in a single-layered monoclinic plate

When it comes to evanescent waves, the wavenumber becomes purely imaginary $\xi = \mathrm{i}\zeta$ wherein ζ is a real number. Note that wavenumber ξ does not relate to the intermediate parameters that only depend on phase velocity v. Thus, studying the dichotomy property of the evanescent waves, under the condition $\Delta \le 0$, can directly start from Eqs. (28)(30)(32)(34) which are the explicit expressions showing the dichotomy properties of the propagating waves for the four cases. Substitution of $\xi = \mathrm{i}\zeta$ into Eqs. (28)(30)(32)(34) and upon simplification via the identical relations $\sinh(\mathrm{i}x) = \mathrm{i}\sin(x)$ and $\cosh(\mathrm{i}x) = \cos(x)$, the dichotomy property of the evanescent waves for the four cases are concluded as follows.

For case 1, all α_1, α_3, α_5 are real numbers.

$$
\begin{aligned}
\mathcal{D}_a(v, \mathrm{i}\zeta) = -\,[&B_1 \sinh(\zeta\alpha_1 h)\cosh(\zeta\alpha_3 h)\cosh(\zeta\alpha_5 h) + B_2 \cosh(\zeta\alpha_1 h)\sinh(\zeta\alpha_3 h)\cosh(\zeta\alpha_5 h) \\
&+ B_3 \cosh(\zeta\alpha_1 h)\cosh(\zeta\alpha_3 h)\sinh(\zeta\alpha_5 h)]P_5 = \mathcal{D}_a^R(v, \zeta) \Rightarrow \mathcal{D}_a^I(v, \zeta) \equiv 0
\end{aligned}
\tag{C.1}
$$

For case 2, only α_1 is a purely imaginary number.

$$\begin{aligned}\mathcal{D}_a(v,\mathrm{i}\zeta) =& -\mathrm{i}[B_1\sin(\zeta a_1 h)\cosh(\zeta\alpha_3 h)\cosh(\zeta\alpha_5 h) + P_2\cos(\zeta a_1 h)\sinh(\zeta\alpha_3 h)\cosh(\zeta\alpha_5 h)\\ &+ P_3\cos(\zeta a_1 h)\cosh(\zeta\alpha_3 h)\sinh(\zeta\alpha_5 h)]P_5 = \mathrm{i}\mathcal{D}_a^I(v,\zeta) \Rightarrow \mathcal{D}_a^R(v,\zeta)\equiv 0\end{aligned} \tag{C.2}$$

For case 3, only α_1, α_3 are purely imaginary numbers.

$$\begin{aligned}\mathcal{D}_a(v,\mathrm{i}\zeta) =& [P_1\sin(\zeta a_1 h)\cos(\zeta a_3 h)\cosh(\zeta\alpha_5 h) + P_2\cos(\zeta a_1 h)\sin(\zeta a_3 h)\cosh(\zeta\alpha_5 h)\\ &- B_3\cos(\zeta a_1 h)\cos(\zeta a_3 h)\sinh(\zeta\alpha_5 h)]P_5 = \mathcal{D}_a^R(v,\zeta) \Rightarrow \mathcal{D}_a^I(v,\zeta)\equiv 0\end{aligned} \tag{C.3}$$

For case 4, all α_1, α_3, α_5 are purely imaginary numbers.

$$\begin{aligned}\mathcal{D}_a(v,\mathrm{i}\zeta) =& -\mathrm{i}[B_1\sin(\zeta a_1 h)\cos(\zeta a_3 h)\cos(\zeta a_5 h) + B_2\cos(\zeta a_1 h)\sin(\zeta a_3 h)\cos(\zeta a_5 h)\\ &+ B_3\cos(\zeta a_1 h)\cos(\zeta a_3 h)\sin(\zeta a_5 h)]P_5 = \mathrm{i}\mathcal{D}_a^I(v,\zeta) \Rightarrow \mathcal{D}_a^R(v,\zeta)\equiv 0\end{aligned} \tag{C.4}$$

Appendix D. The material properties used for the numerical study

For the single-layered monoclinic plate, its material properties are cited from [20] and listed as follows for convenience:

$$\mathbf{C} = \begin{bmatrix} 102.6 & 24.1 & 6.3 & 0 & 0 & 40 \\ & 18.7 & 6.4 & 0 & 0 & 10 \\ & & 13.3 & 0 & 0 & -0.1 \\ & & & 3.8 & 0.9 & 0 \\ & \text{sym} & & & 5.3 & 0 \\ & & & & & 23.6 \end{bmatrix} \text{GPa} \tag{D.1}$$

The mass density is $\rho = 1500\,\mathrm{kg/m^3}$, the plate thickness is $d = 1\,\mathrm{mm}$.

For the $[0]_{50}$ orthotropic laminate, its material properties are cited from [20] and listed as follows for convenience:

$$\mathbf{C} = \begin{bmatrix} 70 & 23.9 & 6.2 & 0 & 0 & 0 \\ & 33 & 6.8 & 0 & 0 & 0 \\ & & 14.7 & 0 & 0 & 0 \\ & & & 4.2 & 0 & 0 \\ & \text{sym} & & & 4.7 & 0 \\ & & & & & 21.9 \end{bmatrix} \text{GPa} \tag{D.2}$$

The mass density is $\rho = 1500\,\mathrm{kg/m^3}$, the plate total thickness is $d = 1\,\mathrm{mm}$.

For the single-layered unidirectional composite plate used to study the instability of TMM, its material properties are cited from [27] and listed as follows for convenience:

$$\mathbf{C} = \begin{bmatrix} 143.8 & 6.2 & 6.2 & 0 & 0 & 0 \\ & 13.3 & 6.5 & 0 & 0 & 0 \\ & & 13.3 & 0 & 0 & 0 \\ & & & 3.6 & 0 & 0 \\ & \text{sym} & & & 5.7 & 0 \\ & & & & & 5.7 \end{bmatrix} \text{GPa} \tag{D.3}$$

The mass density is $\rho = 1560\,\mathrm{kg/m^3}$, the plate thickness is $d = 1\,\mathrm{mm}$.

For the single-layered triclinic plate, its material properties are cited from [39] and listed as follows for convenience:

$$\mathbf{C} = \begin{bmatrix} 185.91 & 93.41 & 136.24 & 14.5 & 8.14 & 8.21 \\ & 207.87 & 109.06 & -23.18 & 16.57 & -16.15 \\ & & 167.7 & 8.68 & -24.72 & 11.28 \\ & & & 59.47 & 5.84 & 16.57 \\ & \text{sym} & & & 100.23 & 14.5 \\ & & & & & 35.11 \end{bmatrix} \text{GPa} \tag{D.4}$$

The mass density is $\rho = 8938.4\,\mathrm{kg/m^3}$, the plate thickness is $d = 2\,\mathrm{mm}$.

References

[1] Rolf Lammering, Ulrich Gabbert, Michael Sinapius, Thomas Schuster, Peter Wierach, Lamb-Wave Based Structural Health Monitoring in Polymer Composites, Springer, 2017.

[2] Victor Giurgiutiu, Structural Health Monitoring of Aerospace Composites, Academic Press, 2015.

[3] Zhongqing Su, Lin Ye, Ye Lu, Guided Lamb waves for identification of damage in composite structures: A review, J. Sound Vib. 295 (3–5) (2006) 753–780.

[4] Michael J.S. Lowe, Matrix techniques for modeling ultrasonic waves in multilayered media, IEEE Trans. Ultrason. Ferroelectr. Freq. Control 42 (4) (1995) 525–542.

[5] Lei Wang, F.G. Yuan, Group velocity and characteristic wave curves of Lamb waves in composites: Modeling and experiments, Compos. Sci. Technol. 67 (7–8) (2007) 1370–1384.

[6] S. Pant, Jeremy Laliberte, Marcias Martinez, B. Rocha, Derivation and experimental validation of Lamb wave equations for an n-layered anisotropic composite laminate, Compos. Struct. 111 (2014) 566–579.
[7] Cai-bin Xu, Zhi-bo Yang, Xue-feng Chen, Shao-hua Tian, Yong Xie, A guided wave dispersion compensation method based on compressed sensing, Mech. Syst. Signal Process. 103 (2018) 89–104.
[8] Yanfeng Shen, Carlos E.S. Cesnik, Hybrid local FEM/global LISA modeling of damped guided wave propagation in complex composite structures, Smart Mater. Struct. 25 (9) (2016) 095021.
[9] Cara AC Leckey, Kevin R Wheeler, Vasyl N Hafiychuk, Halyna Hafiychuk, Doğan A Timuçin, Simulation of guided-wave ultrasound propagation in composite laminates: Benchmark comparisons of numerical codes and experiment, Ultrasonics 84 (2018) 187–200.
[10] Jinsong Yang, Jingjing He, Xuefei Guan, Dengjiang Wang, Huipeng Chen, Weifang Zhang, Yongming Liu, A probabilistic crack size quantification method using in-situ Lamb wave test and Bayesian updating, Mech. Syst. Signal Process. 78 (2016) 118–133.
[11] Ajay Raghavan, Carlos E.S. Cesnik, Finite-dimensional piezoelectric transducer modeling for guided wave based structural health monitoring, Smart Mater. Struct. 14 (6) (2005) 1448.
[12] Emmanuel Lizé, Marc Rébillat, Nazih Mechbal, Christian Bolzmacher, Optimal dual-PZT sizing and network design for baseline-free SHM of complex anisotropic composite structures, Smart Mater. Struct. 27 (11) (2018) 115018.
[13] N. Quaegebeur, P.C. Ostiguy, P. Masson, Correlation-based imaging technique for fatigue monitoring of riveted lap-joint structure, Smart Mater. Struct. 23 (5) (2014) 055007.
[14] Marc Rébillat, Nazih Mechbal, Damage localization in geometrically complex aeronautic structures using canonical polyadic decomposition of Lamb wave difference signal tensors, Struct. Health Monit. 19 (1) (2020) 305–321.
[15] Horace Lamb, On waves in an elastic plate, Proc. R. Soc. A 93 (648) (1917) 114–128.
[16] Norman A. Haskell, The dispersion of surface waves on multilayered media, Bull. Seismol. Soc. Am. 43 (1) (1953) 17–34.
[17] Ameneh Maghsoodi, Abdolreza Ohadi, Mojtaba Sadighi, Calculation of wave dispersion curves in multilayered composite-metal plates, Shock Vib. 2014 (2014).
[18] Anvesh R. Nandyala, Ashish K. Darpe, Satinder P. Singh, Effective stiffness matrix method for predicting the dispersion curves in general anisotropic composites, Arch. Appl. Mech. 89 (9) (2019) 1923–1938.
[19] L. Knopoff, A matrix method for elastic wave problems, Bull. Seismol. Soc. Am. 54 (1) (1964) 431–438.
[20] Darun Barazanchy, Victor Giurgiutiu, A unified formulation for predictive modeling of guided-ultrasonic wave dispersion curves in metallic and composite materials, J. Intell. Mater. Syst. Struct. 28 (10) (2016) 1272–1286.
[21] M. Lowe, B. Pavlakovic, Disperse User's Manual Version 2.0.20a, Imperial College London, London, 2013.
[22] Danny R. Ramasawmy, Ben T. Cox, Bradley E. Treeby, ElasticMatrix: A MATLAB toolbox for anisotropic elastic wave propagation in layered media, SoftwareX 11 (2020) 100397.
[23] Darun Barazanchy, Victor Giurgiutiu, A comparative convergence and accuracy study of composite guided-ultrasonic wave solution methods: Comparing the unified analytic method, SAFE method and DISPERSE, Proc. Inst. Mech. Eng. C 231 (16) (2017) 2961–2973.
[24] Armin M.A. Huber, Markus G.R. Sause, Classification of solutions for guided waves in anisotropic composites with large numbers of layers, J. Acoust. Soc. Am. 144 (6) (2018) 3236–3251.
[25] Luck Wang, S.I. Rokhlin, Stable reformulation of transfer matrix method for wave propagation in layered anisotropic media, Ultrasonics 39 (6) (2001) 413–424.
[26] S.I. Rokhlin, L. Wang, Stable recursive algorithm for elastic wave propagation in layered anisotropic media: Stiffness matrix method, J. Acoust. Soc. Am. 112 (3) (2002) 822–834.
[27] Ayman Kamal, Victor Giurgiutiu, Stiffness transfer matrix method (STMM) for stable dispersion curves solution in anisotropic composites, in: Health Monitoring of Structural and Biological Systems 2014, Vol. 9064, International Society for Optics and Photonics, 2014, 906410.
[28] Joseph L. Rose, Ultrasonic Guided Waves in Solid Media, Cambridge university press, 2014.
[29] Michael J.S. Lowe, Plate Waves for the NDT of Diffusion Bonded Titanium (Ph.D. thesis), Imperial College London, 1992.
[30] Feng Zhu, Bin Wang, Zheng-hua Qian, A numerical algorithm to solve multivariate transcendental equation sets in complex domain and its application in wave dispersion curve characterization, Acta Mech. 230 (4) (2019) 1303–1321.
[31] A. Bernard, M.J.S. Lowe, M. Deschamps, Guided waves energy velocity in absorbing and non-absorbing plates, J. Acoust. Soc. Am. 110 (1) (2001) 186–196.
[32] Feng Zhu, Bin Wang, Zhenghua Qian, Ernian Pan, Accurate characterization of 3D dispersion curves and mode shapes of waves propagating in generally anisotropic viscoelastic/elastic plates, Int. J. Solids Struct. 150 (2018) 52–65.
[33] Christopher Hakoda, Cliff J. Lissenden, Using the partial wave method for wave structure calculation and the conceptual interpretation of elastodynamic guided waves, Appl. Sci. 8 (6) (2018) 966.
[34] Adnan H. Nayfeh, Wave Propagation in Layered Anisotropic Media: With Applications To Composites, Elsevier, 1995.
[35] Yan Li, R. Bruce Thompson, Influence of anisotropy on the dispersion characteristics of guided ultrasonic plate modes, J. Acoust. Soc. Am. 87 (5) (1990) 1911–1931.
[36] Xiang Yan, Fuh-Gwo Yuan, Conversion of evanescent Lamb waves into propagating waves via a narrow aperture edge, J. Acoust. Soc. Am. 137 (6) (2015) 3523–3533.
[37] Victor Giurgiutiu, Mohammad Faisal Haider, Propagating, evanescent, and complex wavenumber guided waves in high-performance composites, Materials 12 (2) (2019) 269.
[38] Maurice Herlihy, Nir Shavit, The Art of Multiprocessor Programming, Revised Reprint, Elsevier, 2012.
[39] F. Hernando Quintanilla, M.J.S. Lowe, R.V. Craster, Modeling guided elastic waves in generally anisotropic media using a spectral collocation method, J. Acoust. Soc. Am. 137 (3) (2015) 1180–1194.